The JCMT BISTRO-2 Survey: Magnetic Fields of the Massive DR21 Filament

The Astrophysical Journal, 941:122 (21pp), 2022 December 20 https://doi.org/10.3847/1538-4357/ac9dfb

The JCMT BISTRO-2 Survey: Magnetic Fields of the Massive DR21 Filament

Tao-Chung Ching[1,2,93], Keping Qiu[3,4], Di Li[2,5,6], Zhiyuan Ren[2], Shih-Ping Lai[7,8], David Berry[9], Kate Pattle[10], Ray Furuya[11,12], Derek Ward-Thompson[13], Doug Johnstone[14,15], Patrick M. Koch[8], Chang Won Lee[16,17], Thiem Hoang[16,17], Tetsuo Hasegawa[18], Woojin Kwon[19,20], Pierre Bastien[21], Chakali Eswaraiah[2,22], Jia-Wei Wang[8], Kyoung Hee Kim[16,23], Jihye Hwang[16,17], Archana Soam[24], A-Ran Lyo[16], Junhao Liu[9], Valentin J. M. Le Gouellec[25,26], Doris Arzoumanian[18], Anthony Whitworth[27], James Di Francesco[14,15], Frédérick Poidevin[28,29], Tie Liu[30], Simon Coudé[31,32], Mehrnoosh Tahani[33,94], Hong-Li Liu[34], Takashi Onaka[35,36], Dalei Li[37], Motohide Tamura[18,36,38], Zhiwei Chen[39], Xindi Tang[37], Florian Kirchschlager[40], Tyler L. Bourke[41,42], Do-Young Byun[16,17], Mike Chen[15], Huei-Ru Vivien Chen[7,8], Wen Ping Chen[43], Jungyeon Cho[44], Yunhee Choi[16], Youngwoo Choi[45], Minho Choi[16], Antonio Chrysostomou[41], Eun Jung Chung[44], Y. Sophia Dai[2], Pham Ngoc Diep[46], Yasuo Doi[47], Yan Duan[2], Hao-Yuan Duan[7], David Eden[48], Lapo Fanciullo[8,49], Jason Fiege[50], Laura M. Fissel[51], Erica Franzmann[50], Per Friberg[9], Rachel Friesen[52], Gary Fuller[42], Tim Gledhill[53], Sarah Graves[9], Jane Greaves[27], Matt Griffin[27], Qilao Gu[30], Ilseung Han[16,17], Saeko Hayashi[54], Martin Houde[55], Charles L. H. Hull[56,57,95], Tsuyoshi Inoue[58], Shu-ichiro Inutsuka[58], Kazunari Iwasaki[59], Il-Gyo Jeong[16,60], Vera Könyves[13], Ji-hyun Kang[16], Miju Kang[16], Janik Karoly[13], Akimasa Kataoka[18], Koji Kawabata[61,62,63], Francisca Kemper[64,65,66], Jongsoo Kim[16,17], Mi-Ryang Kim[16], Shinyoung Kim[16,17], Hyosung Kim[19], Kee-Tae Kim[16,17], Gwanjeong Kim[67], Jason Kirk[13], Masato I. N. Kobayashi[68], Takayoshi Kusune[68], Jungmi Kwon[36], Kevin Lacaille[69,70], Chi-Yan Law[71,72], Sang-Sung Lee[16,17], Hyeseung Lee[44], Jeong-Eun Lee[73], Chin-Fei Lee[8], Yong-Hee Lee[9,73], Guangxing Li[34], Hua-bai Li[71], Sheng-Jun Lin[7], Sheng-Yuan Liu[8], Xing Lu[30], Steve Mairs[9], Masafumi Matsumura[74], Brenda Matthews[14,15], Gerald Moriarty-Schieven[14], Tetsuya Nagata[75], Fumitaka Nakamura[18,76], Hiroyuki Nakanishi[77], Nguyen Bich Ngoc[46,78], Nagayoshi Ohashi[8,9], Geumsook Park[16], Harriet Parsons[9], Nicolas Peretto[27], Felix Priestley[27], Tae-Soo Pyo[54,76], Lei Qian[79], Ramprasad Rao[8], Mark Rawlings[9,80], Jonathan Rawlings[40], Brendan Retter[27], John Richer[81,82], Andrew Rigby[27], Sarah Sadavoy[51], Hiro Saito[83], Giorgio Savini[40], Masumichi Seta[84], Yoshito Shimajiri[18], Hiroko Shinnaga[77], Ya-Wen Tang[8], Kohji Tomisaka[18,76], Le Ngoc Tram[85], Yusuke Tsukamoto[77], Serena Viti[40], Hongchi Wang[39], Jintai Wu[3], Jinjin Xie[2], Meng-Zhe Yang[7], Hsi-Wei Yen[8], Hyunju Yoo[16], Jinghua Yuan[2], Hyeong-Sik Yun[73], Tetsuya Zenko[75], Chuan-Peng Zhang[2,79], Yapeng Zhang[86], Guoyin Zhang[2], Jianjun Zhou[37], Lei Zhu[79], Ilse de Looze[40], Philippe André[87], C. Darren Dowell[88], Stewart Eyres[89], Sam Falle[90], Jean-François Robitaille[91], and Sven van Loo[92]

[1] Research Center for Intelligent Computing Platforms, Zhejiang Lab, Hangzhou 311100, People's Republic of China; chingtaochung@gmail.com
[2] National Astronomical Observatories, Chinese Academy of Sciences, A20 Datun Road, Chaoyang District, Beijing 100012, People's Republic of China
[3] School of Astronomy and Space Science, Nanjing University, 163 Xianlin Avenue, Nanjing 210023, People's Republic of China
[4] Key Laboratory of Modern Astronomy and Astrophysics (Nanjing University), Ministry of Education, Nanjing 210023, People's Republic of China
[5] Department of Astronomy, University of Chinese Academy of Sciences, Beijing 100049, People's Republic of China
[6] NAOC-UKZN Computational Astrophysics Centre, University of KwaZulu-Natal, Durban 4000, South Africa
[7] Institute of Astronomy and Department of Physics, National Tsing Hua University, Hsinchu 30013, Taiwan
[8] Academia Sinica Institute of Astronomy and Astrophysics, No.1, Sec.3., Roosevelt Road, Taipei 10617, Taiwan
[9] East Asian Observatory, 660 N. A'ohōkū Place, University Park, Hilo, HI 96720, USA
[10] Department of Physics and Astronomy, University College London, Gower Street, London WC1E 6BT, UK
[11] Tokushima University, Minami Jousanajima-machi 1-1, Tokushima 770-8502, Japan
[12] Institute of Liberal Arts and Sciences Tokushima University, Minami Jousanajima-machi 1-1, Tokushima 770-8502, Japan
[13] Jeremiah Horrocks Institute, University of Central Lancashire, Preston PR1 2HE, UK
[14] NRC Herzberg Astronomy and Astrophysics, 5071 West Saanich Road, Victoria, BC V9E 2E7, Canada
[15] Department of Physics and Astronomy, University of Victoria, Victoria, BC V8W 2Y2, Canada
[16] Korea Astronomy and Space Science Institute, 776 Daedeokdae-ro, Yuseong-gu, Daejeon 34055, Republic of Korea
[17] University of Science and Technology, Korea, 217 Gajeong-ro, Yuseong-gu, Daejeon 34113, Republic of Korea
[18] National Astronomical Observatory of Japan, National Institutes of Natural Sciences, Osawa, Mitaka, Tokyo 181-8588, Japan
[19] Department of Earth Science Education, Seoul National University, 1 Gwanak-ro, Gwanak-gu, Seoul 08826, Republic of Korea
[20] SNU Astronomy Research Center, Seoul National University, 1 Gwanak-ro, Gwanak-gu, Seoul 08826, Republic of Korea
[21] Centre de recherche en astrophysique du Québec & département de physique, Université de Montréal, 1375, Avenue Thérèse-Lavoie-Roux, Montréal, QC, H2V 0B3, Canada
[22] Indian Institute of Science Education and Research (IISER) Tirupati, Rami Reddy Nagar, Karakambadi Road, Mangalam (P.O.), Tirupati 517 507, India
[23] Department of Physics, College of Natural Science, Ulsan National Institute of Science and Technology (UNIST), 50 UNIST-gil, Ulsan 44919, Republic of Korea
[24] Indian Institute of Astrophysics (IIA), Kormangala, Bangalore 560034, India
[25] SOFIA Science Center, Universities Space Research Association, NASA Ames Research Center, Moffett Field, CA 94035, USA
[26] Université Paris-Saclay, CNRS, CEA, Astrophysique, Instrumentation et Modélisation de Paris-Saclay, F-91191 Gif-sur-Yvette, France
[27] School of Physics and Astronomy, Cardiff University, The Parade, Cardiff, CF24 3AA, UK
[28] Instituto de Astrofísica de Canarias, E-38205 La Laguna,Tenerife, Canary Islands, Spain
[29] Departamento de Astrofísica, Universidad de La Laguna (ULL), Dpto. Astrofísica, E-38206 La Laguna, Tenerife, Spain
[30] Shanghai Astronomical Observatory, Chinese Academy of Sciences, 80 Nandan Road, Shanghai 200030, People's Republic of China
[31] Department of Earth, Environment and Physics, Worcester State University, Worcester, MA 01602, USA
[32] Center for Astrophysics | Harvard & Smithsonian, 60 Garden Street, Cambridge, MA 02138, USA
[33] Dominion Radio Astrophysical Observatory, Herzberg Astronomy and Astrophysics Research Centre, National Research Council Canada, P.O. Box 248, Penticton, BC V2A 6J9, Canada

[34] Yunnan University, Kunming, 650091, People's Republic of China
[35] Department of Physics, Faculty of Science and Engineering, Meisei University, 2-1-1 Hodokubo, Hino, Tokyo 191-8506, Japan
[36] Department of Astronomy, Graduate School of Science, The University of Tokyo, 7-3-1 Hongo, Bunkyo-ku, Tokyo 113-0033, Japan
[37] Xinjiang Astronomical Observatory, Chinese Academy of Sciences, 150 Science 1-Street, Urumqi 830011, Xinjiang, People's Republic of China
[38] Astrobiology Center, National Institutes of Natural Sciences, 2-21-1 Osawa, Mitaka, Tokyo 181-8588, Japan
[39] Purple Mountain Observatory, Chinese Academy of Sciences, 2 West Beijing Road, 210008 Nanjing, People's Republic of China
[40] Department of Physics and Astronomy, University College London, WC1E 6BT London, UK
[41] SKA Observatory, Jodrell Bank, Lower Withington, Macclesfield SK11 9FT, UK
[42] Jodrell Bank Centre for Astrophysics, School of Physics and Astronomy, University of Manchester, Oxford Road, Manchester, M13 9PL, UK
[43] Institute of Astronomy, National Central University, Zhongli 32001, Taiwan
[44] Department of Astronomy and Space Science, Chungnam National University, 99 Daehak-ro, Yuseong-gu, Daejeon 34134, Republic of Korea
[45] Department of Physics and Astronomy, Seoul National University, 1 Gwanak-ro, Gwanak-gu, Seoul 08826, Republic of Korea
[46] Vietnam National Space Center, Vietnam Academy of Science and Technology, 18 Hoang Quoc Viet, Hanoi, Vietnam
[47] Department of Earth Science and Astronomy, Graduate School of Arts and Sciences, The University of Tokyo, 3-8-1 Komaba, Meguro, Tokyo 153-8902, Japan
[48] Armagh Observatory and Planetarium, College Hill, Armagh, BT61 9DB, UK
[49] National Chung Hsing University, 145 Xingda Rd., South Dist., Taichung City 402, Taiwan
[50] Department of Physics and Astronomy, The University of Manitoba, Winnipeg, Manitoba R3T2N2, Canada
[51] Department for Physics, Engineering Physics and Astrophysics, Queen's University, Kingston, ON, K7L 3N6, Canada
[52] National Radio Astronomy Observatory, 520 Edgemont Road, Charlottesville, VA 22903, USA
[53] Department of Physics, Astronomy & Mathematics, University of Hertfordshire, College Lane, Hatfield, Hertfordshire AL10 9AB, UK
[54] Subaru Telescope, National Astronomical Observatory of Japan, 650 N. A'ohōkū Place, Hilo, HI 96720, USA
[55] Department of Physics and Astronomy, The University of Western Ontario, 1151 Richmond Street, London N6A 3K7, Canada
[56] National Astronomical Observatory of Japan, Alonso de Córdova 3788, Office 61B, Vitacura, Santiago, Chile
[57] Joint ALMA Observatory, Alonso de Córdova 3107, Vitacura, Santiago, Chile
[58] Department of Physics, Graduate School of Science, Nagoya University, Furo-cho, Chikusa-ku, Nagoya 464-8602, Japan
[59] Department of Environmental Systems Science, Doshisha University, Tatara, Miyakodani 1-3, Kyotanabe, Kyoto 610-0394, Japan
[60] Department of Astronomy and Atmospheric Sciences, Kyungpook National University, Daegu 41566, Republic of Korea
[61] Hiroshima Astrophysical Science Center, Hiroshima University, Kagamiyama 1-3-1, Higashi-Hiroshima, Hiroshima 739-8526, Japan
[62] Department of Physics, Hiroshima University, Kagamiyama 1-3-1, Higashi-Hiroshima, Hiroshima 739-8526, Japan
[63] Core Research for Energetic Universe (CORE-U), Hiroshima University, Kagamiyama 1-3-1, Higashi-Hiroshima, Hiroshima 739-8526, Japan
[64] Institut de Ciencies de l'Espai (ICE, CSIC), Can Magrans, s/n, E-08193 Bellaterra, Barcelona, Spain
[65] ICREA, Pg. Lluís Companys 23, Barcelona, Spain
[66] Institut d'Estudis Espacials de Catalunya (IEEC), E-08034 Barcelona, Spain
[67] Nobeyama Radio Observatory, National Astronomical Observatory of Japan, National Institutes of Natural Sciences, Nobeyama, Minamimaki, Minamisaku, Nagano 384-1305, Japan
[68] Astronomical Institute, Graduate School of Science, Tohoku University, Aoba-ku, Sendai, Miyagi 980-8578, Japan
[69] Department of Physics and Astronomy, McMaster University, Hamilton, ON L8S 4M1, Canada
[70] Department of Physics and Atmospheric Science, Dalhousie University, Halifax B3H 4R2, Canada
[71] Department of Physics, The Chinese University of Hong Kong, Shatin, N.T., Hong Kong
[72] Department of Space, Earth & Environment, Chalmers University of Technology, SE-412 96 Gothenburg, Sweden
[73] School of Space Research, Kyung Hee University, 1732 Deogyeong-daero, Giheung-gu, Yongin-si, Gyeonggi-do 17104, Republic of Korea
[74] Faculty of Education & Center for Educational Development and Support, Kagawa University, Saiwai-cho 1-1, Takamatsu, Kagawa, 760-8522, Japan
[75] Department of Astronomy, Graduate School of Science, Kyoto University, Sakyo-ku, Kyoto 606-8502, Japan
[76] SOKENDAI (The Graduate University for Advanced Studies), Hayama, Kanagawa 240-0193, Japan
[77] Department of Physics and Astronomy, Graduate School of Science and Engineering, Kagoshima University, 1-21-35 Korimoto, Kagoshima, Kagoshima 890-0065, Japan
[78] Graduate University of Science and Technology, Vietnam Academy of Science and Technology, 18 Hoang Quoc Viet, Cau Giay, Hanoi, Vietnam
[79] CAS Key Laboratory of FAST, National Astronomical Observatories, Chinese Academy of Sciences, People's Republic of China
[80] Gemini Observatory/NSF's NOIRLab, 670 N. A'ohōkū Place, University Park, Hilo, HI 96720, USA
[81] Astrophysics Group, Cavendish Laboratory, J.J. Thomson Avenue, Cambridge CB3 0HE, UK
[82] Kavli Institute for Cosmology, Institute of Astronomy, University of Cambridge, Madingley Road, Cambridge, CB3 0HA, UK
[83] Faculty of Pure and Applied Sciences, University of Tsukuba, 1-1-1 Tennodai, Tsukuba, Ibaraki 305-8577, Japan
[84] Department of Physics, School of Science and Technology, Kwansei Gakuin University, 2-1 Gakuen, Sanda, Hyogo 669-1337, Japan
[85] University of Science and Technology of Hanoi, Vietnam Academy of Science and Technology, 18 Hoang Quoc Viet, Hanoi, Vietnam
[86] Department of Astronomy, Beijing Normal University, Beijing 100875, People's Republic of China
[87] Laboratoire AIM CEA/DSM-CNRS-Université Paris Diderot, IRFU/Service d'Astrophysique, CEA Saclay, F-91191 Gif-sur-Yvette, France
[88] Jet Propulsion Laboratory, M/S 169-506, 4800 Oak Grove Drive, Pasadena, CA 91109, USA
[89] University of South Wales, Pontypridd, CF37 1DL, UK
[90] Department of Applied Mathematics, University of Leeds, Woodhouse Lane, Leeds LS2 9JT, UK
[91] Univ. Grenoble Alpes, CNRS, IPAG, F-38000 Grenoble, France
[92] School of Physics and Astronomy, University of Leeds, Woodhouse Lane, Leeds LS2 9JT, UK
Received 2022 February 3; revised 2022 September 30; accepted 2022 October 25; published 2022 December 21

[93] Jansky Fellow, National Radio Astronomy Observatory, 1003 Lopezville Road, Socorro, NM 87801, USA.
[94] Banting and KIPAC Fellow: Kavli Institute for Particle Astrophysics & Cosmology (KIPAC), Stanford University, Stanford, CA 94305, USA.
[95] NAOJ Fellow.

Abstract

We present 850 μm dust polarization observations of the massive DR21 filament from the *B*-fields In STar-forming Region Observations (BISTRO) survey, using the POL-2 polarimeter and the SCUBA-2 camera on the James Clerk Maxwell Telescope. We detect ordered magnetic fields perpendicular to the parsec-scale ridge of the DR21 main filament. In the subfilaments, the magnetic fields are mainly parallel to the filamentary structures and smoothly connect to the magnetic fields of the main filament. We compare the POL-2 and Planck dust polarization observations to study the magnetic field structures of the DR21 filament on 0.1–10 pc scales. The magnetic fields revealed in the Planck data are well-aligned with those of the POL-2 data, indicating a smooth variation of magnetic fields from large to small scales. The plane-of-sky magnetic field strengths derived from angular dispersion functions of dust polarization are 0.6–1.0 mG in the DR21 filament and ∼0.1 mG in the surrounding ambient gas. The mass-to-flux ratios are found to be magnetically supercritical in the filament and slightly subcritical to nearly critical in the ambient gas. The alignment between column density structures and magnetic fields changes from random alignment in the low-density ambient gas probed by Planck to mostly perpendicular in the high-density main filament probed by James Clerk Maxwell Telescope. The magnetic field structures of the DR21 filament are in agreement with MHD simulations of a strongly magnetized medium, suggesting that magnetic fields play an important role in shaping the DR21 main filament and subfilaments.

Unified Astronomy Thesaurus concepts: Interstellar magnetic fields (845); Star-forming regions (1565); Interstellar filaments (842); Submillimetre astronomy (1647); Polarimetry (1278)

1. Introduction

Recent observations of thermal continuum from dust and molecular lines from gas have revealed that parsec-scale filaments are ubiquitous structures in molecular clouds (André et al. 2014). The collapse and fragmentation of gravitationally unstable filaments host the birth of prestellar cores and protostars (Molinari et al. 2010; Arzoumanian et al. 2011; Hacar et al. 2013; Palmeirim et al. 2013; Fernández-López et al. 2014; Könyves et al. 2015). Further, high-mass star-forming regions are preferentially found in the hubs of filaments, where the longitudinal mass flows along filaments toward the hubs are believed to play a key role in enhancing the density to drive massive star formation (Galván-Madrid et al. 2010; Hill et al. 2011; Hennemann et al. 2012; Liu et al. 2012; Schneider et al. 2012; Peretto et al. 2013; Hacar et al. 2018; Kumar et al. 2020).

Observations of dust polarization at submillimeter/millimeter wavelengths have been proven to be the most efficient method to trace magnetic fields of molecular clouds (Crutcher 2012), given that the emission of magnetically aligned interstellar dust grains is linearly polarized with the polarization angle perpendicular to the direction of local magnetic field projected on the plane of sky (Lazarian & Hoang 2007; Andersson et al. 2015). Single-dish dust polarization surveys reveal magnetic field structures within molecular clouds at resolutions from a few arcmins to tens of arcsecs (e.g., Dotson et al. 2000, 2010; Matthews et al. 2009; Planck Collaboration et al. 2015). Statistical studies of Planck data covering column densities from 10^{20} to 10^{22} cm^{-2} indicate that the low column density structures in diffuse clouds appear to be parallel to the magnetic fields, while the filamentary structures of molecular clouds with high column densities tend to be perpendicular to the magnetic fields (Planck Collaboration et al. 2016a, 2016b). Ground-based telescopes that are capable of resolving magnetic fields in molecular clouds show that, at parsec scale, the magnetic fields of filaments are usually perpendicular to the main axes of filaments (Schleuning 1998; Vallée & Fiege 2006; Matthews et al. 2014; Pattle et al. 2017; Liu et al. 2018; Chuss et al. 2019; Fissel et al. 2019; Soam et al. 2019). The parallel alignment between magnetic fields and low-density subfilaments and the perpendicular alignment between magnetic fields and high-density filaments are also supported by optical and infrared polarization data, indicating that magnetic fields play an important role in filament formation (Alves et al. 2008; Sugitani et al. 2011; Palmeirim et al. 2013; Cox et al. 2016; Soler et al. 2016; Wang et al. 2020). Observations at a few thousand au resolution toward dense cores within filaments, however, reveal complex magnetic fields that are not simply aligned with the structures of cores (Koch et al. 2014; Zhang et al. 2014; Li et al. 2015; Doi et al. 2020; Eswaraiah et al. 2021), indicating a more complex role of magnetic fields in the formation of dense cores.

To study the role of magnetic fields in the formation of filaments and high-mass star-forming cores, we present 850 μm dust polarization observations taken using the James Clerk Maxwell Telescope (JCMT) toward the DR21 filament. The DR21 filament is the densest and most massive region in the Cygnus X complex (Schneider et al. 2016; Cao et al. 2019) at a distance of 1.4 kpc (Rygl et al. 2012). The filament hosts 24 massive dense cores (Motte et al. 2007), including the well-studied massive star-forming regions DR21 and DR21(OH) (Downes & Rinehart 1966). The ridge of the DR21 filament has a length of 4 pc and a total mass of 15,000 $M_\odot$, connected by several subfilaments with masses between 130 $M_\odot$ and 1400 $M_\odot$ (Hennemann et al. 2012). Global infall motions of the filament are suggested by molecular line observations, probably triggered by convergence of flows on cloud scales (Schneider et al. 2010; Csengeri et al. 2011). Embedded clusters of young stellar objects (Kumar et al. 2007), prominent outflows (Davis et al. 2007; Motte et al. 2007; Duarte-Cabral et al. 2013, 2014; Ching et al. 2018), and masers (Braz & Epchtein 1983; Argon et al. 2000; Pestalozzi et al. 2005) are found in the filament, indicating recent high- to intermediate-mass star formation. The active star formation of the DR21 filament could be driven by both the mass accretion through the subfilaments and the converging flows of clouds (Schneider et al. 2010; Hennemann et al. 2012).

The magnetic fields of the DR21 filament have been mapped through single-dish observations of dust polarized emission (100 μm at 35″ resolution (Dotson et al. 2000), 350 μm at 10″ and 20″ resolutions (Kirby 2009; Dotson et al. 2010), 800 μm at 14″ resolution (Minchin & Murray 1994; Greaves et al. 1999), 850 μm at 14″ resolution (Vallée & Fiege 2006; Matthews et al. 2009), 1.1 mm at 19″ resolution (Greaves et al. 1999), and

1.3 mm at 33″ resolution (Glenn et al. 1999)), revealing a uniform structure of magnetic fields at parsec scale that is perpendicular to the filament. Single-dish observations of CN Zeeman measurements at a resolution of 23″ (0.16 pc) found line-of-sight magnetic field strengths of 0.4–0.7 mG in DR21 (OH) (Crutcher et al. 1999; Falgarone et al. 2008), and interferometric HI Zeeman observations at a resolution of 5″ (0.03 pc) found a line-of-sight magnetic field strength of a few tenths of an mG toward the compact H II region of the DR21 core (Roberts et al. 1997). In contrast to the uniform magnetic fields of the filament, interferometric dust polarization observations reveal complex magnetic field structures in the massive dense cores of the filament, suggesting that the magnetic field plays a more important role in the formation of the DR21 filament than in the formation of the cores (Lai et al. 2003; Girart et al. 2013; Ching et al. 2017). A combined analysis of dust polarization data and molecular line data suggests that the gas dynamics arising from gravitational collapse may be the origin of distortion of the magnetic fields in the cores (Ching et al. 2018).

Our observations toward the DR21 filament are part of the extension of the *B*-fields In STar-forming Region Observations (BISTRO) survey (Ward-Thompson et al. 2017). The BISTRO-1 survey carried out POL-2 observations from 2016 to 2019 toward nearby star-forming regions of the Gould Belt clouds, including Orion A (Pattle et al. 2017; Hwang et al. 2021), Ophiuchus (Kwon et al. 2018; Soam et al. 2018; Liu et al. 2019), IC 5146 (Wang et al. 2019), Barnard 1 (Coudé et al. 2019), NGC 1333 (Doi et al. 2020, 2021), Auriga (Ngoc et al. 2021), Taurus (Eswaraiah et al. 2021), Orion B (Lyo et al. 2021), and Serpens (Kwon et al. 2022), aiming to generate a large sample of polarization maps in a uniform and consistent way to study the role of magnetic fields in star formation at scales of a few thousand au. The BISTRO-1 survey was later extended to the BISTRO-2 program for high-mass star-forming regions (M16: Pattle et al. 2018; Rosette: Könyves et al. 2021; NGC 6334: Arzoumanian et al. 2021; Mon R2: Hwang et al. 2022) as well as to the ongoing BISTRO-3 program for various evolutionary stages and environments of star formation. In addition to individual target studies, the BISTRO data have been used to study the polarization properties of dust grains (Pattle et al. 2019; Fanciullo et al. 2022) and the alignment between magnetic fields and outflows (Yen et al. 2021).

This paper is organized as follows: in Section 2, we describe the observations and data reduction; in Section 3, we present the results of the observations; in Section 4, we derive the magnetic field strength and study the relative orientation between magnetic field and filament structure; in Section 5, we discuss our results; and in Section 6, we provide a summary of this paper.

2. Observations

The JCMT polarization observations toward the DR21 filament were made by inserting the POL-2 polarimeter (Bastien et al. 2011; Friberg et al. 2016) into the optical path of the Submillimetre Common-User Bolometer Array 2 (SCUBA-2) camera (Holland et al. 2013). The observations were carried out with 20 sets of 42 minutes integration in Grade 1 weather ($\tau_{225\,\mathrm{GHz}} < 0.05$) from 2017 July to 2020 February as part of the BISTRO-2 program (project ID: M17BL011). The observations were made using the POL-2 DAISY scan mode (Friberg et al. 2016), producing a fully sampled circular region of 12′ diameter. Within the DAISY map, the noise is lowest and close to uniform in the central 3′ diameter region, and increases toward the edge of the map. The Flux Calibration Factors (FCFs) of SCUBA-2 at 850 μm were 516 Jy pW^{-1} beam^{-1} from 2016 November to 2018 June and 495 Jy pW^{-1} beam^{-1} post 2018 June (Mairs et al. 2021). Owing to the transmission losses from POL-2, the FCF of POL-2 is 1.35 times larger than the SCUBA-2 FCF (Dempsey et al. 2013). Weighted by the dates of the observations, the FCF of the POL-2 data toward the DR21 filament is 672 Jy pW^{-1} beam^{-1}. The effective beam size of JCMT is 14.″1 at 850 μm (Dempsey et al. 2013), equivalent to 0.096 pc or 2.0×10^4 au at the distance of DR21 filament.

The data were reduced using the *pol2map* procedure (Parsons et al. 2018; software version on 2020 September 22) within the STARLINK/SMURF package (Jenness et al. 2013; Currie et al. 2014). The details of data reduction with *pol2map* are described in earlier POL-2 works such as Liu et al. (2019) and Wang et al. (2019). In brief, the *pol2map* procedure first creates an initial Stokes *I* map from the POL-2 raw bolometer timestreams. Next, *pol2map* runs a second time with fixed-signal-to-noise-based masks generated from the initial Stokes *I* map to create improved Stokes *I* maps, and it then co-adds the maps into a final Stokes *I* map. Finally, the masks and the final Stokes *I* map are used in a third run of *pol2map* to correct instrumental polarization and produce Stokes *Q* and *U* maps, along with their variance maps, as well as the debiased polarization catalog. The noise levels in the Stokes *Q* and *U* maps are estimated from the Stokes *Q* and *U* variance maps, which are about 3.1 mJy beam^{-1} on the default 4″ pixels of *pol2map*. The average and maximum of the noises in the Stokes *I* map are 3.4 and 13.8 mJy beam^{-1}, respectively. In this paper, we select polarization detections with criteria of $I/\delta I \geqslant 3$, $p/\delta p \geqslant 3$, and $\delta p \leqslant 4\%$ for the uncertainty δI in Stokes *I* emission, the polarization fraction *p*, and the uncertainty δp in *p*. We plot the polarization segments with a 90° rotation to show the magnetic field orientation projected on the plane of the sky (hereafter called magnetic field segments), and we present one magnetic field segment in every two pixels, satisfying the Nyquist sampling of the 14.″1 beam.

To show the improvement of the POL-2 data, we also used the SCUPOL 850 μm polarization data of the DR21 filament. Matthews et al. (2009) built the SCUPOL legacy catalog to provide reference Stokes cubes of comparable quality for 104 star-forming regions, including the observations of the DR21 filament of Vallée & Fiege (2006). We downloaded SCUPOL Stokes *I*, *Q*, and *U* cubes of DR21 from the legacy online catalog.[96] When comparing the POL-2 and SCUPOL data sets, we first regridded the POL-2 data to a pixel size of 10″ to match the SCUPOL map and then used the same criteria of $I/\delta I \geqslant 3$, $p/\delta p \geqslant 3$, and $\delta p \leqslant 4\%$ to select polarization segments for both data sets, instead of the original criteria of $p/\delta p > 2$ in Matthews et al. (2009).

3. Results

3.1. POL-2 Dust Polarization Map

3.1.1. Magnetic Field Morphology

Figure 1 presents the magnetic field segments of the DR21 filament inferred from our POL-2 observations. The detection

[96] https://www.cadc-ccda.hia-iha.nrc-cnrc.gc.ca/en/communi-ty/scupollegacy/

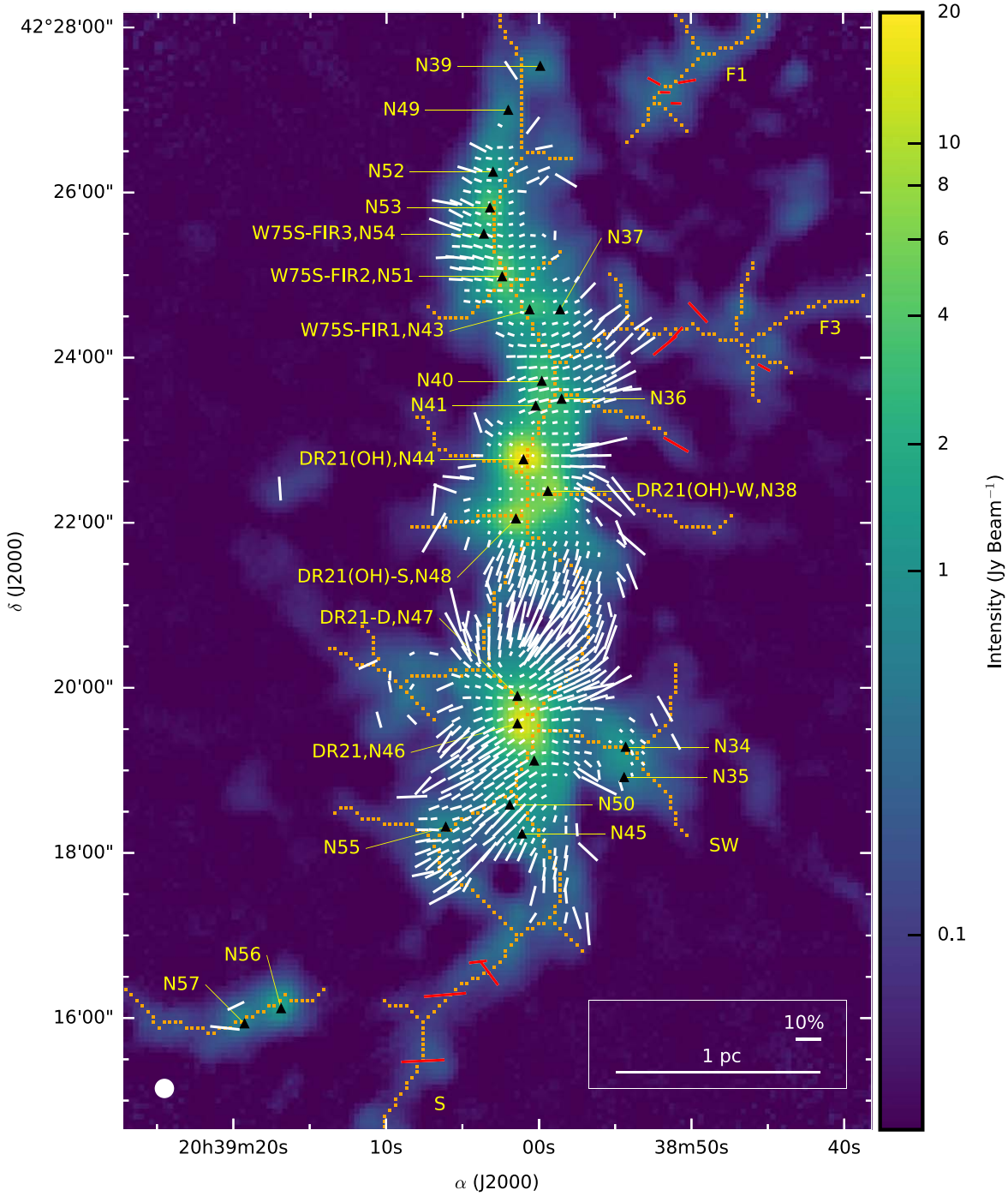

Figure 1. The POL-2 dust polarization map at 850 μm toward the DR21 filament. The color scale represents the Stokes I intensity. The magnetic field segments plotted at intervals of 8″ show the magnetic field orientations, with lengths proportional to the polarization percentages. The JCMT 14.″1 beam is plotted at the bottom left corner. The positions of the 24 massive dense cores in Motte et al. (2007) are marked with filled black triangles and labeled in yellow, and the filamentary structures selected using *filfinder* are marked with orange dots along their crests. The names of the subfilaments following Hennemann et al. (2012) are labeled in yellow. The magnetic field segments of the subfilaments are shown in red color.

of dust polarized emission is more extended than in the results of Vallée & Fiege (2006) and Matthews et al. (2009), owing to the better sensitivity and larger scan area of our observations. The Stokes I emission shows the DR21 main filament elongated in the north–south direction embedded with the bright sources DR21(OH) and DR21 in the middle and in the south of the filament. In the eastern and western sides of DR 21, the two lobes of dust emission extend to a size of about 0.5 pc, comparable to the morphology of the energetic outflows from DR21 (Davis & Smith 1996; White et al. 2010). The western side of the main filament is connected by the east–west elongated F1, F3, and SW subfilaments, and the southern end of the filament is connected by the S subfilament in the southeast direction.

The magnetic field segments in the north of DR21(OH) are mostly horizontal to the filament, implying a parsec-scale magnetic field perpendicular to the main filament. The horizontal magnetic fields are significantly changed to a northwest–southeast

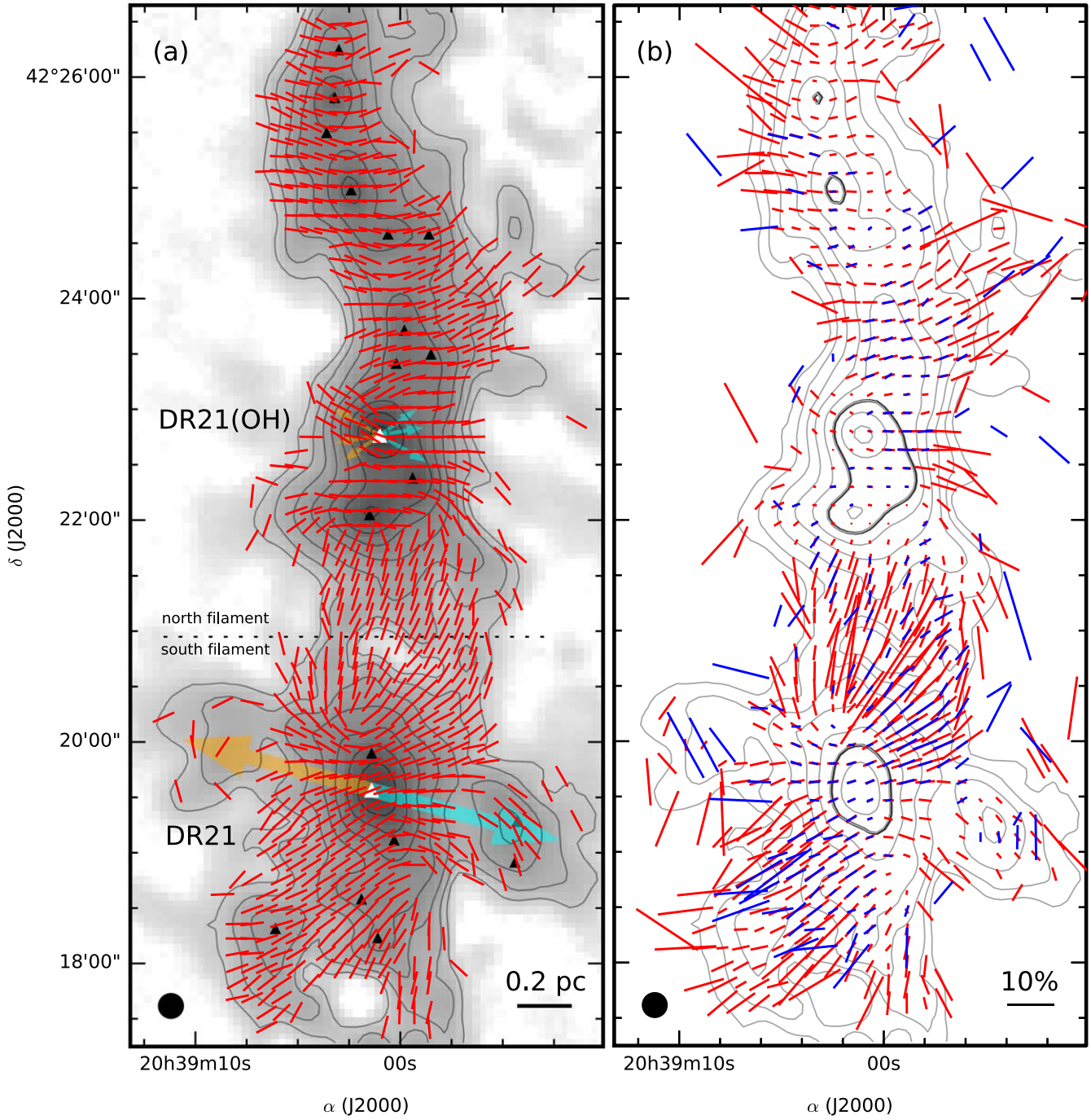

Figure 2. Comparison of the dust polarization maps between POL-2 and SCUPOL observations. (a) The POL-2 polarization map of the main filament. The grayscale represents the Stokes *I* intensity, and the contours show the Stokes *I* emission at levels of 0.125, 0.25, 0.5, 1, 2, 4, 8, and 16 Jy beam^{-1}. The magnetic field segments are the same as those in Figure 1, but plotted with a unified length. The triangles mark the positions of the massive dense cores in Motte et al. (2007), with DR21(OH) in the north and DR21 in the south, highlighted in white color. The dotted line marks the boundary between the north filament and south filament. The orange and cyan arrows represent the directions of the redshifted and blueshifted outflows of DR21(OH) and DR21. Note here that we only show the energetic outflows that might distort the POL-2 magnetic field segments in spite of the large number of outflows from the massive dense cores of the DR21 filament (e.g., Motte et al. 2007; Zapata et al. 2013; Ching et al. 2018). The JCMT 14.″1 beam is plotted at the bottom left corner. (b) The SCUPOL magnetic field segments in blue overlapped with the POL-2 magnetic field segments in red. The length of the segment is proportional to the polarization percentage. The contours are the same as panel (a). The sixth contour at 4 Jy beam^{-1} is emphasized to show the regions with high consistency between the POL-2 and SCUPOL segments.

orientation in the region between DR21(OH) and DR21. The magnetic fields appear to be radial around DR21 and become arc-like in the two lobes of outflows. The arc-like morphologies of dust polarization are similar to those obtained from the imaging polarimetry of H_2 $v = 1$–0 S(1) line, which suggests a helical structure of magnetic fields wrapping around the outflows (Itoh et al. 1999). In the diffuse region, the magnetic fields of the subfilaments are smoothly connected to the magnetic fields of the main filament. At the junctions of the subfilaments and main filament, the magnetic fields appear to be parallel to the structures of the junctions.

Figure 2(a) shows a zoom-in of the polarization map to reveal the detailed magnetic field structures of the main filament. In the north of DR21(OH), the horizontal magnetic

Table 1
Magnetic Field Segments of Subfilaments

$\Delta\alpha$[a] (″)	$\Delta\delta$[a] (″)	PA_B (deg)	PA_f (deg)	$PA_{\lvert B-f\rvert}$[b] (deg)
−92	360	60.5	59.0	1.5
−116	360	−80.3	−51.3	29.0
−100	352	88.5	−45.0	46.5
−108	344	89.5	−38.7	39.2
−124	192	42.8	38.7	4.1
−108	176	−41.5	−68.2	26.7
−100	168	−50.6	−68.2	17.6
−172	152	60.8	21.8	39.0
−108	96	59.7	38.7	21.0
36	−280	−83.1	−51.3	31.8
28	−288	36.7	−51.3	88.0
60	−304	−85.3	−51.3	34.0
76	−352	−87.2	−31.0	56.2

Notes.
[a] With respect to the pointing center at $(\alpha, \delta)_{J2000} = (20^h39^m1\overset{s}{.}1, +42°21'17'')$.
[b] The absolute position angle between PA_B and PA_f in a range [0°, 90°].

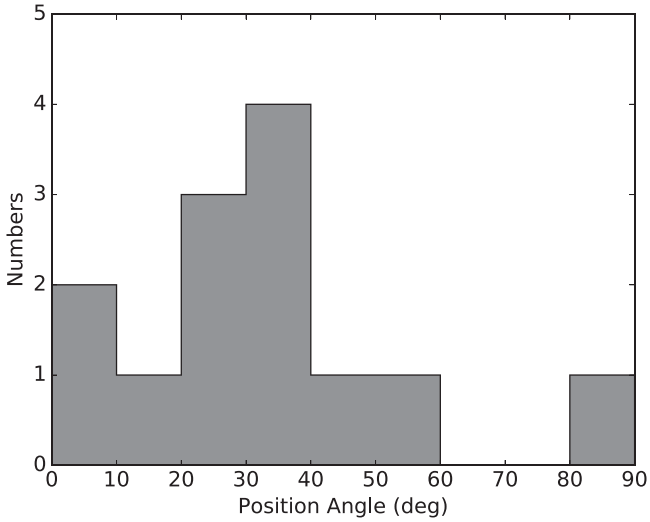

Figure 3. Histogram of position angles ($PA_{\lvert B-f\rvert}$) between the magnetic field segments of subfilaments and the crests of subfilaments in Figure 1. A position angle of 0° means that the magnetic field is parallel to the subfilament crest, and a position angle of 90° means that the magnetic field is perpendicular to the subfilament crest.

fields are inclined in a northeast–southwest orientation in the eastern side of the filament and inclined in a northwest–southeast orientation in the western side. The inclined field morphology in the eastern and western sides of the filament is probably driven by the mass accretion of the filament. In addition, the orientation and morphology of the inclined magnetic fields in the northwest of the main filament appear to be correlated with those of the F1 and F3 subfilaments. The magnetic fields around massive dense cores primarily follow the horizontal magnetic fields of the filament, except for the northeast–southwest oriented magnetic fields around DR21 (OH). The northeast–southwest orientation of the magnetic fields around DR21(OH) are consistent with the small-scale magnetic fields inferred from interferometric observations of dust polarization (Lai et al. 2003; Girart et al. 2013), and we speculate that the distortion of the magnetic fields around DR21(OH) could be driven by the northeast–southwest bipolar outflows of DR21(OH) (White et al. 2010; Zapata et al. 2012; Girart et al. 2013). At the southern end of DR21(OH), the field morphology is slightly northwest–southeast oriented along the connecting bridge between DR21(OH) and DR21. The magnetic field morphology along the connecting bridge is probably regulated by the competitive mass accretion between the two massive cores. Because DR21(OH) is less massive than DR21, the magnetic fields in the southern end of DR21(OH) are pulled toward DR21, generating the fields that are straightened and redirected toward DR21 in a northwest–southeast orientation. The magnetic fields between DR21(OH) and DR21 regulated by competitive mass accretion appear to be similar to the field morphology between the massive cores in the W51 region (Koch et al. 2018). Around DR21, the magnetic fields show a pinched or hourglass morphology with an axis of symmetry along the northwest–southeast direction, consistent with the magnetic field structure inferred from the 350 μm dust polarization observations (Kirby 2009; Dotson et al. 2010).

There are 13 magnetic field segments located in the subfilaments, shown in red segments in Figure 1. We performed the *filfinder* algorithm (Koch & Rosolowsky 2015) to identity the crests of subfilaments with parameters of a global threshold of 30 mJy beam^{-1}, a size threshold of 100 square pixels to extract filaments with length down to 40″ (0.3 pc), and a branch threshold of seven pixels to minimize the length for a subfilament to be two beams. The crests identified by *filfinder* are plotted in Figure 1, and the identifications of subfilaments F1, F3, SW, and S are consistent with those in Kumar et al. (2007) and Hennemann et al. (2012). In Table 1, we list the positions, the position angles of magnetic fields (PA_B), the position angles of subfilaments (PA_f), and the absolute position angles ($PA_{\lvert B-f\rvert}$) between PA_B and PA_f of the 13 magnetic field segments of subfilaments. The PA_f is determined by the five pixels of crests that are closest to the magnetic field segment. Figure 3 shows the histogram of $PA_{\lvert B-f\rvert}$. The histogram of the position angles has more samples between 0° and 45° than between 45° and 90°, indicating that the magnetic fields tend to be parallel to the crests of subfilaments, different from the perpendicular alignment between the magnetic fields and the DR21 main filament. The parallel alignment between magnetic fields and subfilaments revealed in our POL-2 data is in agreement with the comparison of Herschel and Planck data that trace the S subfilament and magnetic fields at a larger scale (Hu et al. 2021).

3.1.2. Polarization Properties

Figure 4 compares the polarization fraction p with the Stokes I intensity for each of the POL-2 segments in Figure 1. There is an overall decreasing correlation of p with increasing I, and the low-intensity data have a steeper slope in the p–I correlation than the high-intensity data. In addition, the polarization fractions of several low-intensity data exceed the observed maximum polarization fraction of $22^{+3.5}_{-1.4}$% of the Planck 850 μm data (Planck Collaboration et al. 2020) as well as the predicted maximum polarization fraction of ∼15% of the submillimeter emission from interstellar dust grains (Draine & Fraisse 2009). The steep slope of p–I correlation and large polarization fractions (>20%) of low-intensity data can be found in other POL-2 observations (e.g., Kwon et al. 2018; Soam et al. 2018; Coudé et al. 2019; Pattle et al. 2019; Wang et al. 2019; Arzoumanian et al. 2021). When the missing flux in

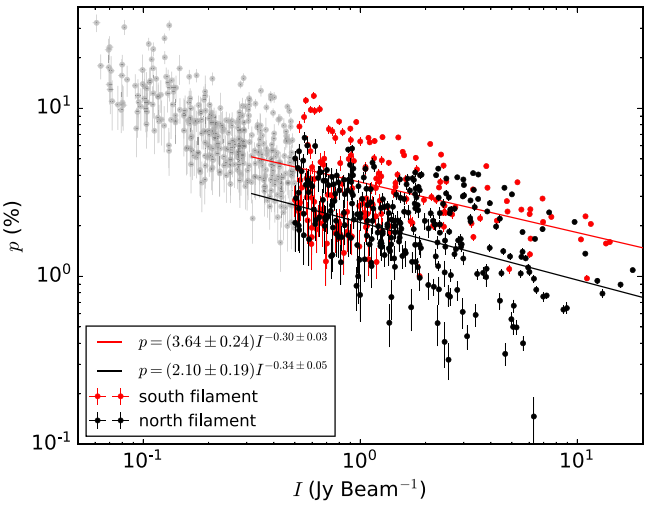

Figure 4. Polarization fraction p as a function of Stokes I intensity. The gray dots represent the low-intensity data ($I < 0.5$ Jy beam^{-1}). The black and red dots represent the high-intensity data ($I \geqslant 0.5$ Jy beam^{-1}) of the north filament and south filament, respectively. The best-fit models of the p–I correlations of the north and south filaments are shown by the black and red lines, respectively.

Stokes I data is more severe than those in Stokes Q and U data, the missing flux issue can lead to a polarization fraction larger than the intrinsic value. The steep p–I correlation and the large polarization fractions of low-intensity data thus indicate that the low-intensity data suffer more Stokes I missing flux than the high-intensity data (see Section 3.3 for a further analysis of the total and polarized missing flux in POL-2 data).

For the high-intensity data ($I \geqslant 0.5$ Jy beam^{-1}) in Figure 4, the polarization fractions of the segments in the north of the filament surrounding DR21(OH) are lower than those in the south of the filament surrounding DR21 (see Figure 2(a) for the separation boundary around the saddle region of the main filament). To study the p–I correlation, we use an empirical power-law model (Tamura et al. 1987) with

$$p(I) = p_1 \left(\frac{I}{\text{Jy beam}^{-1}} \right)^{-\alpha}, \quad (1)$$

where p_1 is the polarization fraction at 1 Jy beam^{-1}. The best-fit model of the north filament gives $\alpha = 0.34 \pm 0.05$ and $p_1 = (2.10 \pm 0.19)\%$, and the best-fit model of the south filament gives $\alpha = 0.30 \pm 0.03$ and $p_1 = (3.64 \pm 0.24)\%$. The difference of 0.04 between the α of the north filament and the α of the south filament is less than the uncertainty of 0.06 in the difference, whereas the difference of 1.54% between the p_1 of the north and the p_1 of the south filaments is about five times larger than the uncertainty of 0.31% in the difference. The consistent values of α indicate that the dust grains of the north and south filaments have a similar property, and the significant difference in the values of p_1 suggests that the Stokes I missing flux of the south filament is larger than the north filament, perhaps owing to differences in the intensities or spatial scales of the diffuse emission in the north and south filaments.

The values of α inferred from POL-2 observations of several molecular clouds are usually from 0.5 to 0.9 (IC 5146: $0.56^{+0.27}_{-0.34}$ (Wang et al. 2019), Barnard 1: 0.85 ± 0.01 (Coudé et al. 2019), Ophiuchus B: 0.86 ± 0.03 (Pattle et al. 2019), Ophiuchus C: 0.83 ± 0.03 (Pattle et al. 2019), Auriga: 0.82 ± 0.03 (Ngoc et al. 2021), Rosette: 0.49 ± 0.08 (Könyves et al. 2021), Serpens: 0.634 (Kwon et al. 2022)). The 0.30–0.34 shallow values of α of the DR21 filament are similar to the values of 0.34 ± 0.02 for Ophiuchus A (Pattle et al. 2019), 0.36 ± 0.04 for Orion B (Lyo et al. 2021), and 0.35 ± 0.02 for NGC 6334 (Arzoumanian et al. 2021). The shallow α can be explained by the more evolved nature of the DR21 filament. According to modern grain alignment theory (Lazarian & Hoang 2007; Hoang & Lazarian 2016; Hoang et al. 2021), dust grains are aligned by radiative torques, and the grain alignment toward the highest intensity is caused by internal radiation from the massive central star. As a result, the embedded sources of DR21 and DR21(OH) may increase the alignment efficiency in the high-density regions, producing a shallower α than those found in clouds without embedded sources.

3.2. Comparison between POL-2 and SCUPOL Results

Figure 2(b) compares the polarization maps of our POL-2 data with the SCUPOL data of Matthews et al. (2009). The noise level in the SCUPOL Stokes Q and U maps is about 13 mJy beam^{-1}, and that of the POL-2 data regridded to 10″ pixel is about 2.2 mJy beam^{-1}. Above the sixth contour at 4 Jy beam^{-1} intensity, the two data sets are approximately consistent in both polarization angles and polarization degrees. Below the sixth contour, the differences between the two data sets become larger. In the region between DR21(OH) and DR21 and in the southeast region of DR21, the differences in polarization angles can be as large as 50°, and the differences in polarization degrees can be as large as 15%. There are 215 pairs of spatially overlapping segments between the two data sets. Figure 5 shows the comparisons of polarization angles and polarization degrees for the overlapping segments. The polarization angles and polarization degrees of the segments satisfying $I \geqslant 4$ Jy beam^{-1} show a better agreement between the two data sets than the segments weaker than 4 Jy beam^{-1}. The mean values of the absolute differences in polarization angles and polarization degree of the segments satisfying $I \geqslant 4$ Jy beam^{-1} are 8°.8 and 0.50%, and those values of the segments satisfying $I < 4$ Jy beam^{-1} are 18°.4 and 2.7%.

We further performed the two-sample Kolmogorov–Smirnov (KS) test to compare the likelihood of the POL-2 and SCUPOL polarization angles in Figure 5(a). When using all the data points, the KS statistic is 10.2% and the probability that the two samples have the same distribution at a KS significance level 0.05 is 19.9%. When using the data points with $I \geqslant 4$ Jy beam^{-1}, the KS statistic is 29.2% and the probability rises to 21.6%, indicating that the POL-2 and SCUPOL sets have likely originated from the same distribution only for the high-intensity data points. The probability of the DR21 filament data is higher than the probabilities of 6% in the Ophiuchus C cloud (Liu et al. 2019) and 0.6% in the Barnard 1 cloud (Coudé et al. 2019). The best consistency between the POL-2 and SCUPOL data has been found so far in the Ophiuchus B cloud with a probability of 90.5% (Soam et al. 2018). The KS test indicates that the consistency between the POL-2 and SCUPOL maps is better for the magnetic field segments with stronger I intensities, and the improvement of POL-2 from SCUPOL in the DR21 filament is similar to the improvement of POL-2 data in other clouds. Considering that the sensitivity of our POL-2 data is about three times better than the SCUPOL data, the POL-2 segments are more reliable than the SCUPOL segments.

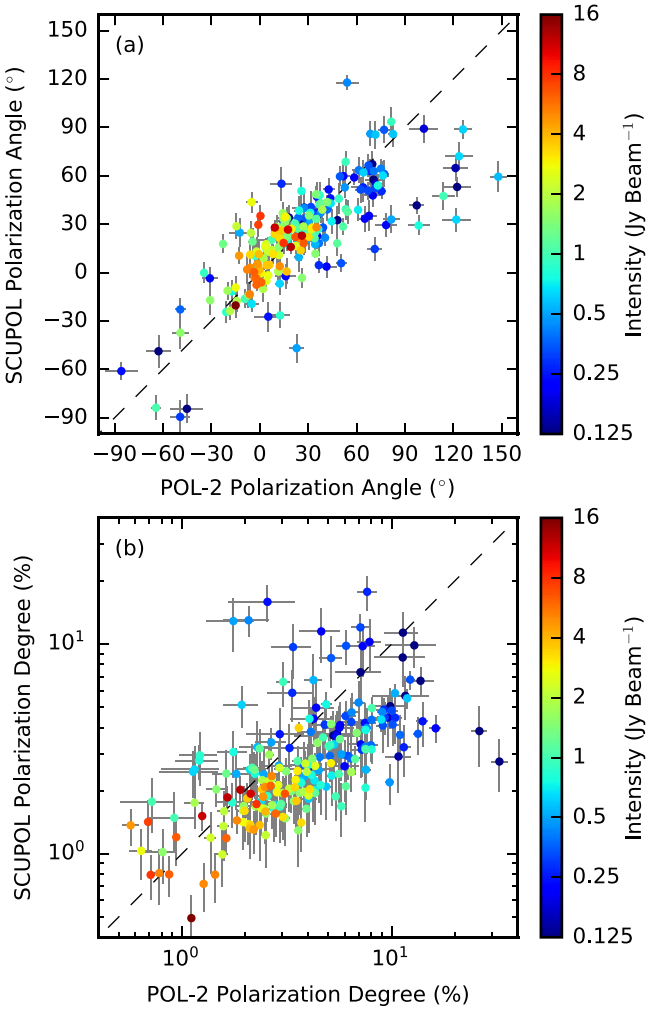

Figure 5. Comparisons of polarization angles and polarization degrees of the 215 overlapping POL-2 and SCUPOL segments in Figure 2(b). The color scale represents the Stokes I intensity of the data. To properly compare the polarization angles of POL-2 and SCUPOL data (i.e., the absolute difference between the two data sets should be less than 90°) and perform a KS test, some of the polarization angles are shifted from a range of [−90°, 90°] to a range of [0°, 180°].

The p–I correlation using the SCUPOL 439 polarization segments of DR21 filament gives $\alpha = 0.50 \pm 0.01$ (Poidevin et al. 2013). Considering that the distribution of the SCUPOL polarization segments is more extended than the lowest contour at 0.125 Jy beam^{-1} in Figure 2(b), the α derived from the SCUPOL data might be biased by the missing flux issue in the low-intensity data and therefore is steeper than our values of $\alpha = 0.30$–0.34.

3.3. Global Magnetic Fields Inferred from the Planck Data

Planck 850 μm (353 GHz) polarization data are used to study the large-scale magnetic fields of the DR21 filament at the 5′ (∼2.0 pc) resolution of the Planck beam. The 2015 release of Planck HFI maps (PR2; Planck Collaboration I et al. 2016), where the monopole of the cosmic infrared background has been subtracted (Planck Collaboration VIII et al. 2016), were obtained from the Planck Legacy Archive.[97] To compare the Planck and JCMT results, we transform the polarization angles

[97] http://pla.esac.esa.int/pla/#home

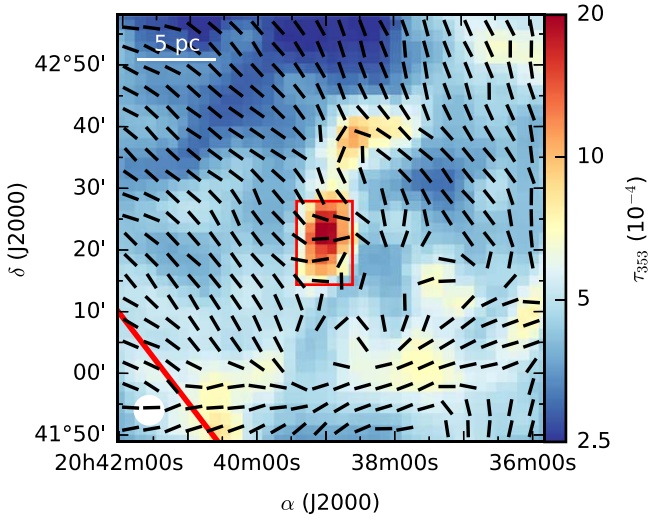

Figure 6. Planck 850 μm magnetic field segments overlaid on the τ_{353} map toward the DR21 filament. The black segments represent the magnetic field orientations with a unified length. The red box at the center marks the area of Figure 1. At the bottom left corner, the red stripe represents the galactic disk plane, and the Planck 5′ beam is shown.

of Planck data that are originally obtained in galactic coordinates into the polarization angles in equatorial coordinates by computing the angle ψ between the equatorial north and the galactic north. For epoch J2000,

$$\psi = \arctan\left[\frac{\cos(l - 32.^{\circ}9)}{\cos b \cot 62.^{\circ}9 - \sin b \sin(l - 32.^{\circ}9)}\right], \quad (2)$$

where l and b are the galactic coordinates of the object (Corradi et al. 1998; see this work's Appendix for the derivation).

Figure 6 shows the large-scale magnetic fields inferred from Planck polarization data satisfying $p/\delta p \geqslant 3$ overlaid on the map of dust optical depth at 353 GHz (τ_{353}) in Planck Collaboration XI et al. (2014). The DR21 filament is the most prominent object in this 30 pc × 30 pc map, even though DR21 is close to the galactic disk plane at $b \sim 0.^{\circ}6$. The diffuse regions on the east and north sides and in the northwest corner of the map show a fairly regular global magnetic field with a northeast–southwest orientation, parallel to the galactic disk plane. This regular field is distorted in the medium above an intermediate optical depth of $\tau_{353} \sim 7 \times 10^{-4}$ in the south of the map, probably owing to the active star-forming activity of the Cygnus X complex. Toward the DR21 filament, a bent morphology of magnetic fields is notable: the northeast–southwest oriented global field is bent to an east–west orientation in the middle of the filament and bent to a northwest–southeast orientation in the south end of the filament, consistent with the main features of the magnetic fields of the DR21 filament at the 0.1 pc resolution of Figure 1. The polarized flux in the 1.′7-sized central pixel of Figure 6 is 3.81 mK$_{\rm CMB}$ × $1.'7^2$ = 253 mJy, and the integrated POL-2 polarized flux over the identical area after smoothing Figure 1 to a resolution of 5′ is 240 mJy. The consistency of the Planck polarized flux and POL-2 polarized flux indicates that the east–west oriented magnetic field at the center of Figure 6 is primarily traced by the polarized emission of the filament rather than by the polarized emission of the diffuse region. Therefore, the bent morphology of large-scale magnetic fields toward the DR21 filament is associated with the 0.1 pc scale magnetic

fields of the filament rather than a distortion of large-scale magnetic fields in the diffuse region.

The Stokes I flux in the central pixel of Figure 6 is 0.525 $K_{CMB} \times 1.'7^2 = 34.9$ Jy, whereas the integrated POL-2 Stokes I flux over the identical area is 18.2 Jy. The missing large-scale flux of the POL-2 Stokes I data is more severe than those of the Stokes Q and U data. A similar trend of more flux being missing in Stokes I than in Q and U is found in the POL-2 and Planck data of NGC 1333 (Doi et al. 2020). The POL-2 Stokes I missing flux of NGC 1333 is 13% of the Planck flux, and the missing flux of filament DR21 is 48%. The missing flux of the POL-2 data comes from the background subtraction of atmospheric signal in the *pol2map* procedure, making POL-2 data not sensitive to diffuse emission with spatial scales larger than the size of the observed region. Because the diffuse emission of DR21 filament is stronger than that of NGC 1333, the missing flux of DR21 filament hence is larger than the missing flux of NGC 1333. In Figure 5(b), the polarization degrees of the POL-2 data are preferentially larger than those of the SCUPOL data, contrary to the general results of POL-2 data having polarization degrees slightly smaller than those of SCUPOL data (Soam et al. 2018; Doi et al. 2020). Again, the large POL-2 polarization degrees of the DR21 filament are likely caused by the large missing Stokes I flux in the POL-2 data.

4. Analysis

4.1. Angular Dispersion Function

4.1.1. Formalism

To estimate the magnetic field strength in molecular clouds from dust polarization observations, the Davis–Chandrasekhar–Fermi (hereafter DCF; Davis 1951; Chandrasekhar & Fermi 1953) equation is the most widely used method. The DCF equation assumes that the ratio of turbulence to magnetic field strength would lead to a similar level of variation in the magnetic fields as well as in the velocities, $\delta B/B \simeq \delta V_{\rm los}/V_{\rm A}$, where B is the strength of the magnetic field, δB is the variation about B, $\delta V_{\rm los}$ is the velocity dispersion along the line of sight, and $V_{\rm A} = B/\sqrt{4\pi\rho}$ is the Alfvén speed at density ρ. Because dust polarization segments trace the plane-of-sky component of magnetic field, the variation in the plane-of-sky magnetic field strength is expected to be proportional to the measured dispersion of polarization angles, i.e., $\delta B/B_{\rm pos} \sim \delta\Phi$. Consequently, the DCF equation can be written as

$$B_{\rm pos} = F\sqrt{4\pi\rho}\,\frac{\delta V_{\rm los}}{\delta\Phi}, \tag{3}$$

where F is a correction factor usually assumed to be $\sim$0.5, accounting for the smoothing of magnetic fields along the line of sight and the inadequate spatial resolution of dust polarization observations (Heitsch et al. 2001; Ostriker et al. 2001; Padoan et al. 2001).

To avoid inaccurate estimation of $\delta B/B_{\rm pos}$ from simply taking the dispersion of polarization angles, refinements of the DCF equation with more sophisticated statistical analyses have been made. Hildebrand et al. (2009) proposed a structure function analysis of the polarization angle difference between every pair of polarization segments in a given map as a function of the segment separation. In this structure function analysis, the plane-of-sky magnetic field is assumed to be composed of a large-scale ordered component B_0 and a small-scale turbulent component B_t, and the ratio of B_0 to B_t can be fitted without any a priori assumptions about the turbulence in the cloud or the morphology of the large-scale field. Houde et al. (2009) proposed an angular dispersion function method to expand the structure function analysis by including the signal integration across the telescope beam and through the line-of-sight depth of the source. Recently, the method of Houde et al. (2009) has become well-recognized in deriving magnetic field strength from dust polarization maps of single-dish observations (Chuss et al. 2019; Coudé et al. 2019; Liu et al. 2019; Soam et al. 2019; Wang et al. 2019; Eswaraiah et al. 2020; Guerra et al. 2021) and numerical simulations (Liu et al. 2021).

Houde et al. (2009) suggest that, if the correlation length δ for B_t is much smaller than the thickness of the cloud Δ', the ratio of B_t to B_0 can be evaluated from the angular dispersion function in the form

$$1 - \langle \cos[\Delta\Phi(l)]\rangle \simeq \frac{1}{N_{\rm cell}}\frac{\langle B_t^2\rangle}{\langle B_0^2\rangle} \times [1 - e^{-l^2/2(\delta^2+2W^2)}] + \sum_{j=1}^{\infty} a'_{2j} l^{2j}, \tag{4}$$

where $\Delta\Phi(l)$ is the polarization angle difference between polarization segments separated by a distance l, W is the beam width (i.e., the FWHM beam divided by $\sqrt{8\ln 2}$), the summation is a Taylor expansion representing the structure in B_0 that does not involve turbulence, and $N_{\rm cell}$ is the number of turbulent cells along the line of sight obtained by

$$N_{\rm cell} = \frac{(\delta^2 + 2W^2)\Delta'}{\sqrt{2\pi}\,\delta^3}. \tag{5}$$

The turbulence component in the angular dispersion function is

$$b^2(l) = \frac{1}{N_{\rm cell}}\frac{\langle B_t^2\rangle}{\langle B_0^2\rangle} e^{-l^2/2(\delta^2+2W^2)}. \tag{6}$$

Because B_t is the source of perturbation in B_0, the $\langle B_t^2\rangle/\langle B_0^2\rangle$ derived from Equation (4) provides a good approximation of the $\delta B/B_{\rm pos}$ in the DCF equation for evaluating the magnetic field strength on the plane of sky as

$$B_{\rm pos} = \sqrt{4\pi\rho}\,\delta V_{\rm los}\left[\frac{\langle B_t^2\rangle}{\langle B_0^2\rangle}\right]^{-1/2}. \tag{7}$$

4.1.2. Angular Dispersion Function of the JCMT and Planck Data

Figure 7 shows the angular dispersion functions of the JCMT and Planck data toward the DR21 filament. Because the main features of horizontal POL-2 segments in the north of the filament are notably different from those of the radial POL-2 segments in the south of the filament, we perform the analysis separately for the POL-2 segments in the north filament (Figure 7(a)) and in the south filament (Figure 7(b)). The numbers of segment pairs reach a maximum at $l = 80''$ for the POL-2 data and at $l = 30'$ for the Planck data, implying that the angular dispersion functions are fully sampled below $80''$ for the JCMT map and fully sampled below $30'$ for the Planck map. Here, we focus on the fully sampled data points. The POL-2 angular dispersion function in the north filament is slightly smaller than that in the south filament, indicating that the magnetic fields in the north are more ordered than those in the south. Owing to limited angular resolution, the

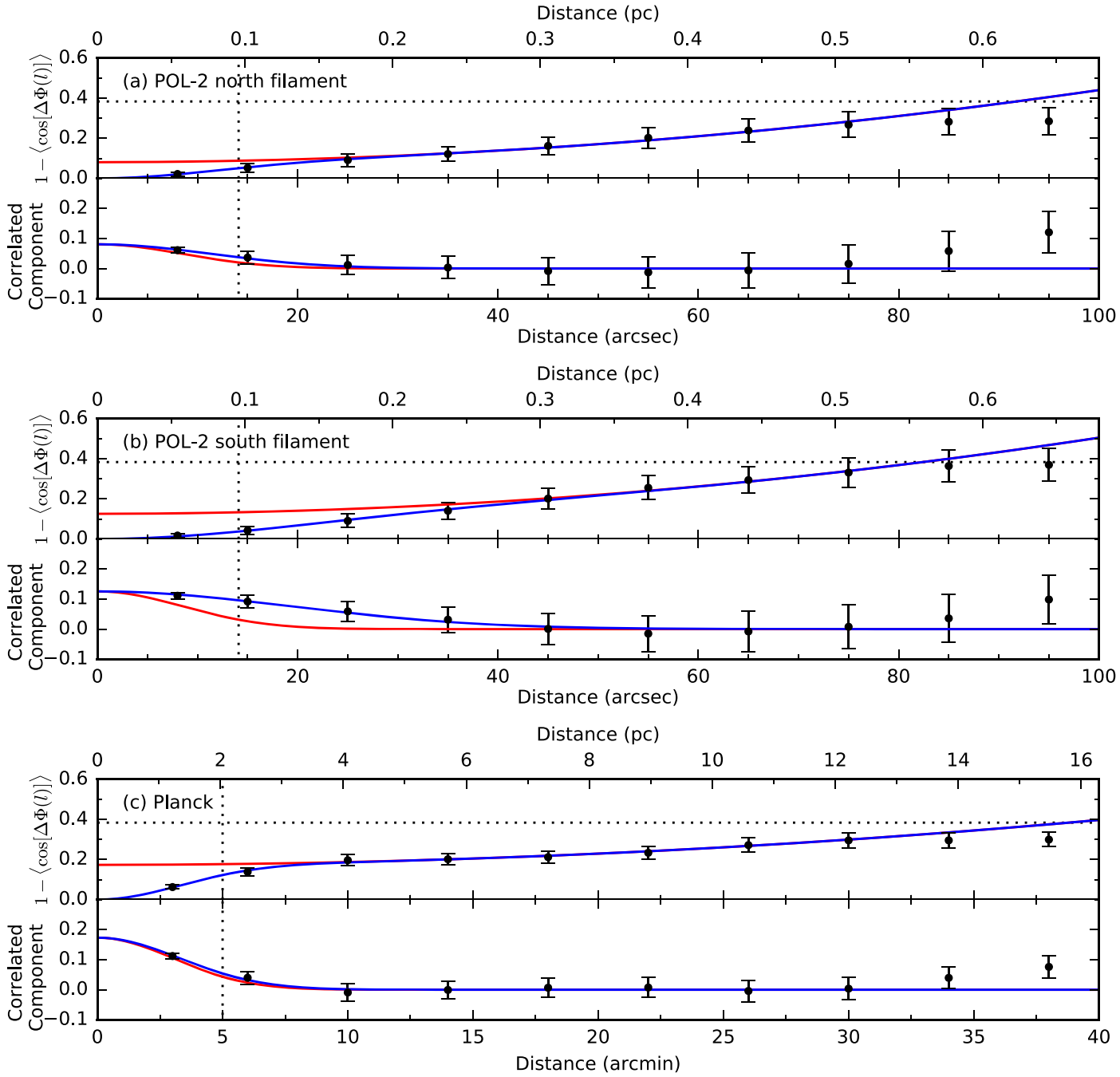

Figure 7. Dispersion analysis of the POL-2 and Planck polarization segments toward the DR21 filament. For each source, the analysis of the angular dispersion function is plotted in the top panel, and the correlated component of the dispersion function is plotted in the bottom panel. Top panels: the dots represent the mean values of the data, and the error bars show the standard deviations of the mean values. The blue line shows the best fit to the data (Equation (4)), and the red line shows the ordered component $a_2' l^2 + b^2(0)$ of the best fit. The dotted vertical and horizontal lines denote the beam size and the expected value for random magnetic fields, respectively. Bottom panels: the dots represent the correlated component of the best fit to the data. The blue line shows the turbulent component $b^2(l)$ of the best fit, and the red line shows the correlation due to the beam (i.e., $b^2(l)$ when $\delta = 0$).

angular dispersion function is close to zero when the length scale l is smaller than the beam. At scales above the beams, the angular dispersion functions of POL-2 and Planck data are both at a level between 0.2 and 0.3, indicating that the ratio of ordered to turbulent magnetic fields remains similar from small to large scales. In addition, all the angular dispersion functions of the POL-2 and Planck data are below the angular dispersion of a random field ($1 - \cos 52^\circ = 0.384$; Poidevin et al. 2010), indicating that the magnetic fields of the DR21 filament are distinctly not random.

We use the nonlinear least-squares Marquardt–Levenberg algorithm[98] to fit the parameters of δ, $\langle B_t^2\rangle / \langle B_0^2\rangle$, and a_{2j}' in Equation (4). The DR21 main filament and subfilaments derived from the Herschel map have a mean central width of about 0.34 pc (Hennemann et al. 2012), and we use the width as the effective thickness Δ' for both the JCMT and Planck data, assuming that the DR21 main filament is similar to an edge-on cylinder and its thickness is close to its width. We only

[98] The `scipy.optimize` package of python.

Table 2
Angular Dispersion Function Fit Parameters

Data	δ (pc)	$\langle B_t^2\rangle/\langle B_0^2\rangle$	a_2' (arcsec^{-2})	$N_{\rm cell}$	n (cm^{-3})	$\delta V_{\rm los}$[a] (km s^{-1})	$B_{\rm pos}$[b] (mG)	λ[c]
POL-2 North	$(51 \pm 10) \times 10^{-3}$	0.49 ± 0.17	$(3.6 \pm 0.3) \times 10^{-5}$	6.1 ± 2.6	4.0×10^5	1.0	0.63 ± 0.18	3.9
POL-2 South	$(117 \pm 21) \times 10^{-3}$	0.18 ± 0.02	$(3.8 \pm 0.7) \times 10^{-5}$	1.4 ± 0.4	4.0×10^5	1.0	1.04 ± 0.13	2.4
Planck	1.02 ± 0.16	0.27 ± 0.16	$(4.0 \pm 0.6) \times 10^{-5}$	1.6 ± 0.9	2.0×10^4	0.7	0.13 ± 0.04	0.9

Notes.
[a] Values from single-dish $H^{13}CO^+$ 1–0 observations (Schneider et al. 2010).
[b] Assume 10% uncertainty in n and $\delta V_{\rm los}$ to estimate the uncertainty in $B_{\rm pos}$.
[c] Obtained with $B_{\rm pos} = \frac{\pi}{4}B$.

fit the fully sampled data points, and the parameters a_{2j}' are reduced to first order a_2' because the fitting range is small. The best fits of the angular dispersion functions are shown in Figure 7, and the fitted parameters are listed in Table 2. The correlation lengths δ of the POL-2 north segments, POL-2 south segments, and Planck segments are $7\farcs5 \pm 1\farcs5$, $17\farcs3 \pm 3\farcs1$, and $2\farcm5 \pm 1\farcm4$, respectively (see Table 2 for the δ in parsec). Except for the POL-2 north filament, the correlation lengths are not resolved by the beams. The $N_{\rm cell}$ and $\langle B_t^2\rangle/\langle B_0^2\rangle$ of the sources are between 1.4 and 6.1 and between 0.2 and 0.5, respectively. Both the $N_{\rm cell}$ and $\langle B_t^2\rangle/\langle B_0^2\rangle$ suggest that the magnetic fields more ordered than disturbed by turbulence, as the POL-2 segments in Figure 2 are dominated by ordered magnetic fields perpendicular to the main filament and the Planck segments in Figure 6 are dominated by ordered magnetic fields parallel to the galactic disk plane.

To derive the magnetic field strength using Equation (7), we adopt column densities of 41.6×10^{22} cm^{-2} for the main filament and $\sim 2 \times 10^{22}$ cm^{-2} (note this value is consistent with the density derived from the Planck data in Figure 9) for the diffuse region obtained from the DR21 Herschel map (Hennemann et al. 2012) with $\Delta' = 0.34$ pc to derive the number densities n of the POL-2 and Planck maps, using $\rho = \mu m_{\rm H} n$ where $\mu = 2.86$ is the mean molecular weight (Kirk et al. 2013; Pattle et al. 2015) and $m_{\rm H}$ is the atomic mass of hydrogen.

We estimate the $\delta V_{\rm lsr}$ from the velocity dispersion (σ) of the $H^{13}CO^+$ 1–0 data at an angular resolution of 29″, because the emission of $H^{13}CO^+$ is well-correlated with the dust emission in the DR21 filament (Schneider et al. 2010). The derived $B_{\rm pos}$ strengths are $\sim$0.6 mG in the north filament, $\sim$1.0 mG in the south filament, and $\sim$0.1 mG in the diffuse region. Our value of the north filament is consistent with the SCUPOL results of $B_{\rm pos} = 0.78$ mG derived using the DCF method (Equation (3)) in Vallée & Fiege (2006) and $B_{\rm pos} = 0.62$ mG derived from the angular dispersion function analysis in Girart et al. (2013). However, our value is about six times weaker than the 2.8–3.9 mG in Poidevin et al. (2013) using the structure function analysis of Hildebrand et al. (2009), mainly owing to Poidevin et al. (2013) assuming a value of n that is 10 times larger than ours. Our $B_{\rm pos}$ for the south filament is lower by a factor of three than the values from 2.5 to 3.1 mG derived using the DCF method from 350 μm polarization data by Kirby (2009). The difference between the two works is primarily owed to Kirby (2009) using a velocity dispersion of 4.2 km s^{-1} from the HCN 4–3 line toward the DR21 core, which is about four times larger than what we used. From Equations (4) and (5), $1 - \langle \cos[\Delta\Phi(l)]\rangle$ is proportional to $1/\Delta' \times \langle B_t^2\rangle/\langle B_0^2\rangle$, and hence Δ' and $\langle B_t^2\rangle/\langle B_0^2\rangle$ are coupled. Considering that our assumption of $\Delta' = 0.34$ pc of the diffuse region is an underestimation, $\langle B_t^2\rangle/\langle B_0^2\rangle$ is also underestimated. Therefore, our value of 0.13 mG in the diffuse region could be an upper limit of $B_{\rm pos}$ in the Planck data.

4.2. Histogram of Relative Orientations

4.2.1. Formalism

Dust polarization orientations in molecular clouds often show correlations with the intensity gradients inferred from the dust continuum contours (Goodman et al. 1990; Chapman et al. 2011; Koch et al. 2012). We quantify the relative orientation of the magnetic field with respect to the column density structures of the DR21 filament using the histogram of relative orientations (HRO; Soler et al. 2013). In the HRO technique, the relative orientation angle ϕ between the magnetic field and the tangent to the column density contour is evaluated using

$$\phi = \arctan\left(\frac{\boldsymbol{B} \times \nabla N}{\boldsymbol{B} \cdot \nabla N}\right), \tag{8}$$

where $\boldsymbol{B}$ is the magnetic field orientation inferred from the polarization map and ∇N is the gradient of column density, used to characterize the column density structures. Although the range of arctan function is $[-90°, 90°]$, we use a range $[0°, 90°]$ for ϕ without loss of generality as suggested in Soler et al. (2017), because the relative orientation is independent of the reference and thus ϕ is equivalent to $-\phi$. The convention of ϕ is equivalent to the $|90° - \delta|$ in Koch et al. (2013) that $\phi = 0°$ indicates that the magnetic field is parallel to the tangent of the column density contour (perpendicular to the column density gradient), and $\phi = 90°$ indicates that the magnetic field is perpendicular to the tangent of the column density contour (parallel to the column density gradient).

To obtain an HRO, the gradients of a column density map and the magnetic field segments of a polarization map are first compared pixel by pixel to produce a map of ϕ. Next, the map of ϕ is divided into bins of column densities containing an equal number of segments, and an HRO is generated for each bin to examine the change in ϕ with increasing column densities. For maps with small uncertainties in column densities and polarization angles, the typical propagated error in ϕ is usually less than 10°. Hence, by presenting an HRO with angle bins of a width larger than the error in ϕ, the uncertainty in the HRO is dominated by the histogram binning process. The

variance in the kth histogram bin is given by

$$\sigma_k^2 = h_k\left(1 - \frac{h_k}{h_{\rm tot}}\right), \quad (9)$$

where h_k is the number of samples in the kth bin and $h_{\rm tot}$ is the total number of samples (Planck Collaboration et al. 2016b).

To evaluate the preferential relative orientation in each column density bin, the shape of the HRO is quantified using a histogram shape parameter ξ, defined as

$$\xi = \frac{A_0 - A_{90}}{A_0 + A_{90}}, \quad (10)$$

where A_0 is the area under the histogram in the range $0° < \phi < 22.°5$ and A_{90} is the area under the histogram in the range $67.°5 < \phi < 90°$ (Soler et al. 2017). An HRO peaking at $\phi = 0°$ would have $\xi > 0$, an HRO peaking at $\phi = 90°$ would have $\xi < 0$, and a flat HRO would have $\xi \sim 0$. The uncertainty in ξ is obtained from

$$\sigma_\xi^2 = \frac{4(A_{90}^2\sigma_{A_0}^2 + A_0^2\sigma_{A_{90}}^2)}{(A_0 + A_{90})^4}, \quad (11)$$

where $\sigma_{A_0}^2$ and $\sigma_{A_{90}}^2$ represent the variances of the areas, characterizing the "jitter" of the histograms. The value of ξ is nearly independent of the number of angle bins selected to represent the histogram if the bin widths are smaller than the integration range, but the jitter does depend on the number of angle bins in the histogram. If the jitter is large, σ_ξ is large compared to $|\xi|$, and the relative orientation is indeterminate (Planck Collaboration et al. 2016b).

Finally, analyses of HROs characterize the trend of the relative orientation between magnetic fields and column density structures of a cloud from its low- to high-density regions with a linear regression between ξ and atomic gas column density N(H) (Planck Collaboration et al. 2016b):

$$\xi = C_{\rm HRO}[\log_{10}(N({\rm H})/{\rm cm}^{-2}) - X_{\rm HRO}]. \quad (12)$$

4.2.2. Histogram of Relative Orientations of the JCMT and Planck Data

In order to further compare the analyses of HROs of Planck and JCMT data from low-density to high-density regimes, we construct the column density maps of the data. To convert the JCMT dust continuum map to a column density map, we calculate the column density $N(H_2)$ of molecular gas as follows:

$$N({\rm H}_2) = \frac{\gamma I_\nu}{\mu m_{\rm H}\kappa_\nu B_\nu(T)}, \quad (13)$$

where γ is the gas-to-dust ratio of 100, I_ν is the Stokes I intensity at frequency ν, $\kappa_\nu = 1.5$ cm^2 g^{-1} is the dust opacity at 850 μm of cool and dense dust mantles (Ossenkopf & Henning 1994), and $B_\nu(T)$ is the Planck function at the dust temperature T of 15 K previously measured in the DR21 filament (Hennemann et al. 2012). To scale the Planck τ_{353} map to a column density map, we calculate the column density N(H) of atomic gas following the dust opacity relation found using Galactic extinction measurements of quasars (Planck Collaboration XI et al. 2014):

$$\tau_{353}/N({\rm H}) = 1.2 \times 10^{-26}\ {\rm cm}^2. \quad (14)$$

We next calculate the gradients of the $N(H_2)$ and N(H) maps using the Gaussian derivatives method described in Soler et al. (2013). To obtain gradients at the pixels of the POL-2 and Planck magnetic field segments in Figures 1 and 6, we apply a 3×3 derivative kernel over the grid of pixels illustrating magnetic field segments. Because the gradients in this grid are computed over two FWHM beams for both the JCMT and Planck data, obtaining gradients using this method guarantees adequate sampling of gradients.

Figures 8 and 9 show the gradient segments of the column density maps and the maps of ϕ of the JCMT and Planck data. The majority of POL-2 segments in the DR21 main filament tend to be parallel ($\phi = 90°$) to the gradient segments with $N(H_2) \gtrsim 10^{23}$ cm^{-2}. In the low column density regions of the JCMT map, the alignment between POL-2 segments and gradient segments becomes less significant. The large-scale magnetic field segments and gradient segments in the Planck map appear to be more randomly aligned than the small-scale segments in the JCMT map. The uncertainty in the position angle of the gradient is determined by the derivative of the noise in the column density map (Planck Collaboration et al. 2016b). Because the respective noise levels in the POL-2 Stokes I map and the Planck τ_{353} map are much less than a few percent of the I map and τ_{353} values, the uncertainties in the gradient directions are typically less than 1°. We use a selection criterion of $p/\delta p \geqslant 3$ for the magnetic field segments, corresponding to an uncertainty less than 10° in polarization angle (Naghizadeh-Khouei & Clarke 1993). Therefore, we expect that the errors in ϕ are less than 10°.

We divide the 765 measurements of ϕ of the POL-2 data into five $N(H_2)$ bins and the 371 measurements of ϕ of the Planck data into three N(H) bins to calculate HROs. Figures 10 and 11 plot the HROs of the JCMT and Planck data using six angle bins each of 15° width. The HROs reveal different kinds of relative orientations between magnetic fields and column density contours of the JCMT and Planck data. The JCMT HRO of the lowest $N(H_2)$ bin increases slightly from $\phi = 0°$ to $\phi = 90°$, and the HROs of the intermediate and highest $N(H_2)$ bins show prominent peaks at 90°, suggesting a trend from a weak perpendicular orientation of ϕ in regions with $N(H_2) \lesssim 10^{22.5}$ cm^{-2} to a strong perpendicular orientation of ϕ for $N(H_2) \gtrsim 10^{22.5}$ cm^{-2} in the DR21 main filament. In contrast, the Planck HROs are flat for all three of the N(H) bins, suggesting no preferential orientation of ϕ in the large-scale diffuse region of the DR21 filament.

Figure 12 presents the measurements of ξ in different N(H) bins derived from the HROs of the JCMT and Planck data. To compare the ξ of the two data sets, the column density $N(H_2)$ is transferred to the N(H) assuming $2 \times N(H_2) = N$(H). The ξ of the three Planck N(H) bins are consistently close to zero with a relatively large value of σ_ξ. The ξ of the lowest JCMT N(H) bin is slightly smaller than the ξ of the three Planck bins. Considering that the σ_ξ of the four data points are relatively large and the missing flux of the POL-2 Stokes I measurement (see Section 3.3) might cause the lowest JCMT N(H) bin to be smaller than its intrinsic column density, the ξ of the JCMT data seems to agree with the ξ of the Planck data. The ξ for the

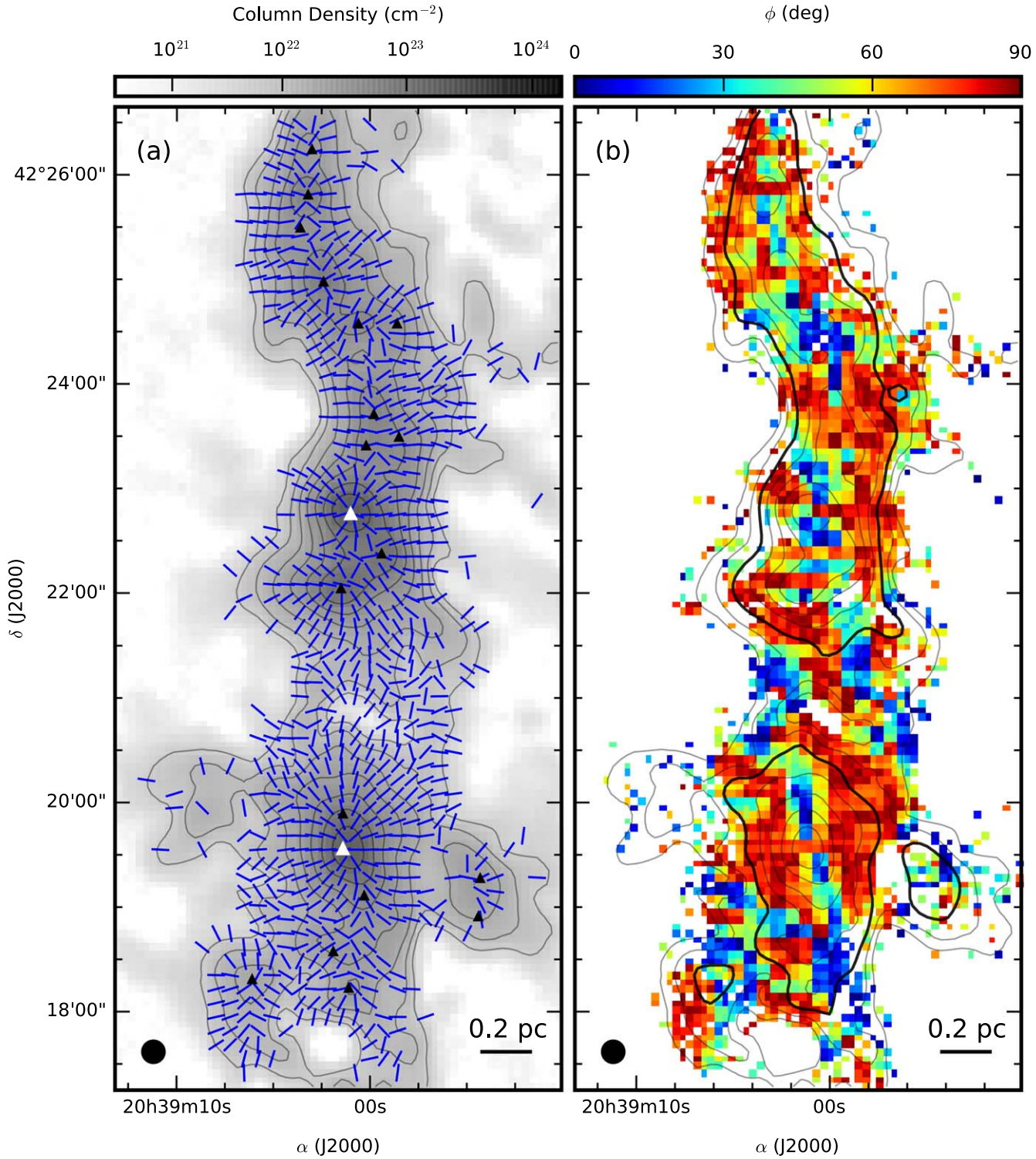

Figure 8. Comparison of the magnetic field segments and column density gradient segments of the POL-2 data. (a) $N(H_2)$ column density map derived from the JCMT Stokes I emission overlaid with the gradient segments calculated by convolving the column density map with a Gaussian derivative kernel. The contours show the $N(H_2)$ at levels of 0.125, 0.25, 0.5, 1, 2, 4, 8, and 16×10^{23} cm^{-2}. The length of the gradient segments is normalized. The gradient segments shown here are those overlaid with the magnetic field segments in Figure 2(a). (b) The map of relative orientation angle ϕ between the magnetic field segments in Figure 2(a) and the gradient segments in panel (a) here. The contours are the same as panel (a), with the contour at 5×10^{22} cm^{-2} emphasized to show the transition from no preferential orientation of ϕ in low-density regions to perpendicular orientation of ϕ in high-density regions.

rest of the JCMT N(H) bins are broadly negative, indicating a strong preference for perpendicular alignment between the small-scale magnetic fields and the ridge of the DR21 filament (parallel alignment between magnetic fields and density gradients).

5. Discussion

5.1. The Role of Magnetic Field in the DR21 Filament

One of the important parameters required to evaluate the role of magnetic fields in star formation is the dimensionless

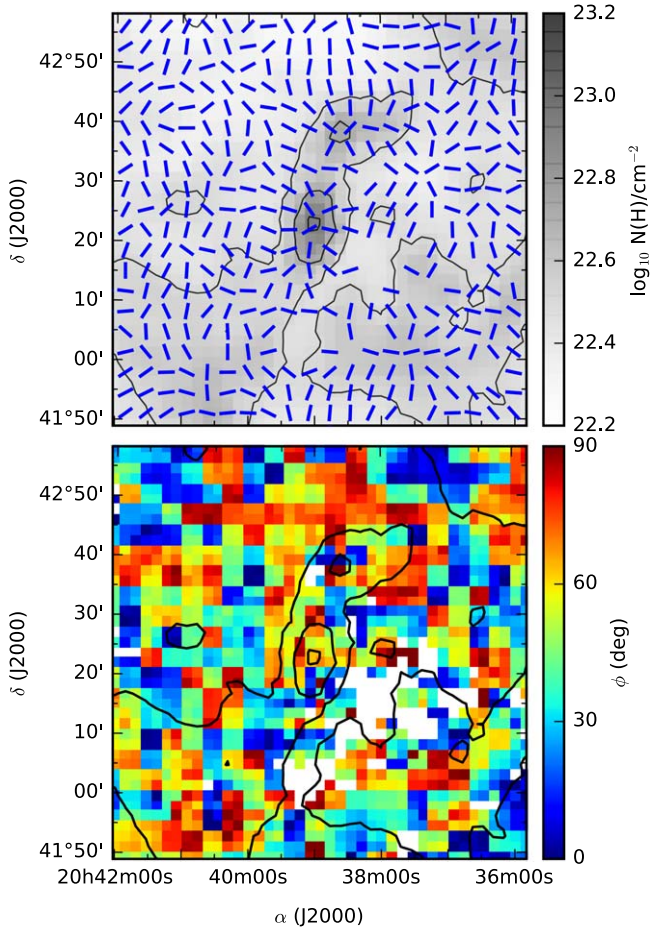

Figure 9. Comparison of the magnetic field segments and column density gradient segments of the Planck data. Top panel: $N(H_2)$ column density map derived from the Planck τ_{353} map overlaid with the gradient segments calculated by convolving the column density map with a Gaussian derivative kernel. The contours show the $N(H_2)$ at levels of 2, 4, 8, and 16×10^{22} cm^{-2}. The length of the gradient segments is normalized. The gradient segments shown here are those overlaid with the magnetic field segments in Figure 6. Bottom panel: The map of relative orientation angle ϕ between the magnetic field segments in Figure 6 and the gradient segments in the top panel.

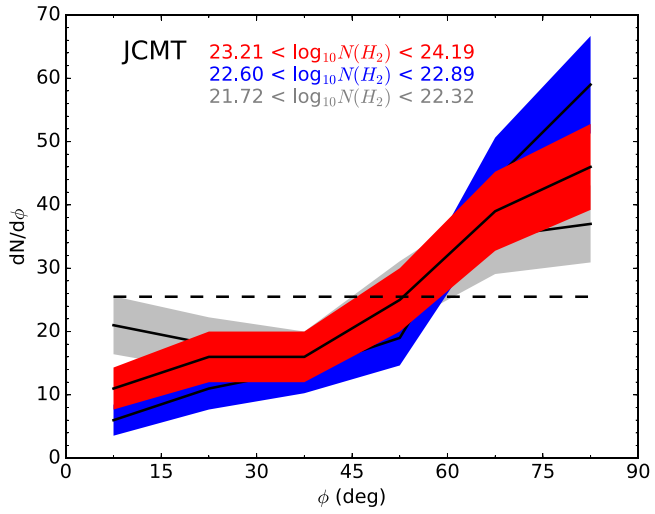

Figure 10. HROs for the lowest, the intermediate, and the highest $N(H_2)$ bins (gray, blue, and red, respectively) of the JCMT data. The horizontal dashed line corresponds to the average HRO per angle bin of 15° for an $N(H_2)$ bin. The widths of the shaded areas for each histogram correspond to the ± 1 σ_k uncertainties (Equation (9)) related to the histogram binning operation.

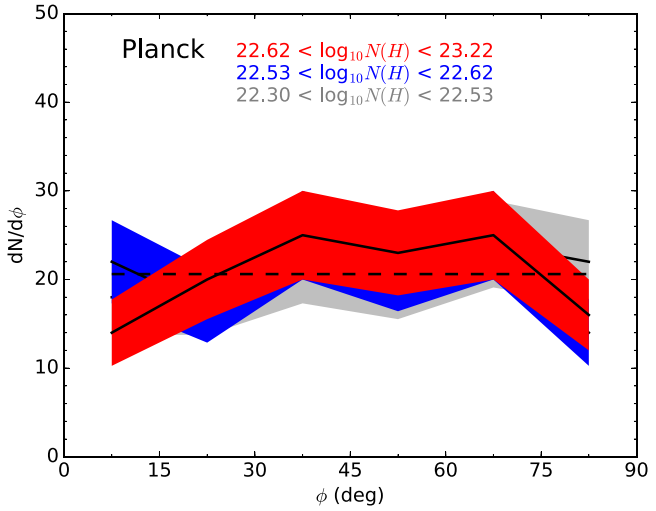

Figure 11. HROs for the lowest, the intermediate, and the highest $N(H)$ bin (gray, blue, and red, respectively) of the Planck data. The horizontal dashed line corresponds to the average HRO per angle bin of 15° for an $N(H)$ bin. The widths of the shaded areas for each histogram correspond to the ± 1 σ_k uncertainties (Equation (9)) related to the histogram binning operation.

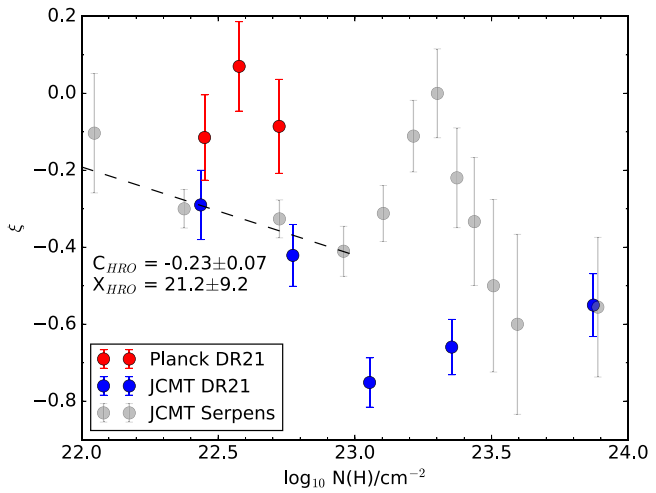

Figure 12. Relative orientation parameter ξ, defined in Equations (10) and (11), calculated for the different $N(H)$ bins of the Planck (red) and JCMT (blue) data of the DR21 filament. The JCMT results of ξ in the Serpens Main region are shown in gray dots. The black dashed line and the values of $C_{\rm HRO}$ and $H_{\rm HRO}$ correspond to the linear fit of Equation (12) for the JCMT data below $N(H) = 10^{23}$ cm^{-2}.

mass-to-flux ratio λ, which refers to the ratio of the mass in a magnetic flux tube to the magnitude of magnetic flux (Crutcher et al. 2004). In units of its critical value of $2\pi G^{1/2}$, $\lambda = 7.6 \times 10^{-21}[N(H_2)/\mathrm{cm}^{-2}][B/\mu\mathrm{G}]^{-1}$. In the theory of magnetically dominated star formation (Shu et al. 1987; Mouschovias & Ciolek 1999), clouds are initially magnetically subcritical ($\lambda < 1$), and to become a star-forming region, magnetic supercriticality ($\lambda > 1$) of a cloud is required for the self-gravity to overwhelm the magnetic support and form stars through gravitational collapse. Using the statistically most probable value of $B_{\rm pos} = \frac{\pi}{4}B$ (Crutcher et al. 2004) and the column density obtained from the Herschel map (see Section 4.1.2), the λ values of the main filament and diffuse region are listed in Table 2. Given the uncertainties in the column densities, in the $B_{\rm pos}$, and in the projection correction from $B_{\rm pos}$ to B, we estimate that the uncertainty in λ would be

as large as half of the value. The λ values of the main filament are about 2.4–3.9, consistent with the value of 3.4 obtained using SCUPOL data (Girart et al. 2013) and the value of 2–3 obtained using the CN Zeeman measurements toward DR21 (OH) (Crutcher et al. 1999). The λ of the diffuse region is 0.9, however, which should be taken as a lower limit because the $B_{\rm pos}$ of the diffuse region could be overestimated.

These λ imply different roles of magnetic fields in the main filament and the surrounding diffuse region. The significant supercriticality of the main filament implies that self-gravity dominates magnetic fields and the filament is undergoing gravitational collapse, in agreement with the infall motions of the filament suggested from molecular line observations (Schneider et al. 2010; Csengeri et al. 2011). Meanwhile, the observed perpendicular alignment between the main filament and magnetic fields is consistent with the MHD simulations of a strongly magnetized medium in which a magnetic field can regulate mass flows along field lines to form parsec-scale filamentary structures perpendicular to magnetic fields (e.g., Nakamura & Li 2008; Inoue & Fukui 2013; Chen & Ostriker 2014; Li & Klein 2019). In contrast, the λ of the diffuse region is slightly subcritical or nearly critical, indicating that the ambient gas is incapable of forming the DR21 filament through direct gravitational collapse. Considering that the column densities of the subfilaments are between those of the diffuse region and main filament, the λ values of subfilaments should be larger than that of the diffuse region and smaller than that of the main filament. In other words, the subfilaments might be the places where the transition from subcriticality to supercriticality occurs. The subfilaments of DR21 appear to be parallel to the parsec-scale magnetic fields and perpendicular to the main filament. These features are similar to the striations around filamentary clouds in MHD simulations formed via Alfvén waves (Heyer et al. 2008; Tritsis & Tassis 2018) or Kelvin–Helmholtz instability (Chen et al. 2017; Li & Klein 2019).

The magnetic fields of the DR21 filament seem to play a more important role on large scales and become less important on small scales. At scales of a few parsecs, the magnitude of magnetic flux is comparable to self-gravity, preventing the collapse of ambient gas. For the parsec-scale main filament, the magnetic fields are important in shaping the filamentary structure, even though the magnetic fields are overwhelmed by the self-gravity of the filament. The magnetic fields of six massive dense cores, including DR21(OH), in the filament have been studied in Girart et al. (2013) and Ching et al. (2017) using dust polarization observations at resolutions of a few thousand au. In contrast to the ordered parsec-scale magnetic fields that are perpendicularly aligned to the filament, the magnetic fields of those cores have complex structures that appear to be randomly aligned to the core structures. The λ of the cores are supercritical with values comparable to that of the main filament, but the ratio of virial kinematic energy to virial magnetic energy of the cores is at least an order of magnitude larger than that of the filament. Meanwhile, molecular line observations suggest that increasing kinetic energy in the core comes from gravitational collapse and might be the source of the distortion of the magnetic fields into complex structures (Ching et al. 2018). Hence, the massive cores appear to be weakly magnetized, and self-gravity and gas dynamics are more important than magnetic fields in the formation of massive dense cores. Down to scales of $\sim$1000 au, the study of fragmentation of 18 massive dense cores, including three cores in the DR21 filament, suggests that the correlation between the fragmentation levels and the number densities of the cores is stronger than the correlation between the fragmentation levels and the λ of the cores (Palau et al. 2021).

5.2. Comparison of the HROs of the DR21 Filament and Other Clouds

The HRO of the Serpens Main region of the BISTRO survey has been studied in Kwon et al. (2022). In Figure 12, the ξ measurements of the Serpens Main region are overlaid on those of the DR21 filament. Both the DR21 and the Serpens Main data show a turning point of ξ around N(H) of 10^{23} cm^{-2}. Owing to the displacement in column density between the JCMT and Planck data, we select the ξ of the JCMT data below $N(\mathrm{H}) = 10^{23}$ cm^{-2} to derive the $C_{\rm HRO}$ and $X_{\rm HRO}$ in Equation (12). The resulting $C_{\rm HRO}$ of -0.23 reflects the trend that ξ changes from a value close to zero in the low N(H) bins to negative values in the high N(H) bins. The resulting $X_{\rm HRO}$ of 21.2, equivalent to 1.58×10^{21} cm^{-2}, corresponds to a characteristic column density where ξ changes its sign, or in other words, a boundary where the relative orientation between the column density structures and magnetic fields changes from a more random orientation in low-density regions to a nonrandom, preferentially perpendicular orientation in high-density regions.

The HROs of 10 nearby Gould Belt molecular clouds (at distances of less than 450 pc, namely Taurus, Ophiuchus, Lupus, Chamaeleon–Musca, Corona Australis, Aquila Rift, Perseus, IC 5146, Cepheus, and Orion) have been measured using the Planck data smoothed to 10′ resolution (Planck Collaboration et al. 2016b). The ξ of the HROs are found to decrease with increasing N(H), indicating field orientation from preferentially parallel or having no preferred orientation at the lowest $N(\mathrm{H}) \sim 10^{21}$ cm^{-2} of the data to preferentially perpendicular at the highest $N(\mathrm{H}) \sim 10^{22.5}$ cm^{-2} of the data. Except for the Corona Australis cloud that shows an almost flat slope of ξ, the $C_{\rm HRO}$ of the other nine clouds have a range from -0.22 to -0.68, and the $X_{\rm HRO}$ have a range from 21.67 to 22.70. The HROs of the 10 clouds and the high-latitude cloud L1642 have further been studied between the N(H) derived from Herschel data at 20″ resolution and the magnetic fields inferred from Planck 850 μm polarization data, and negative slopes of ξ versus N(H) have been identified (Malinen et al. 2016; Soler 2019). Besides the Planck polarization data, the HRO analysis applied to the BLASTPol data at 250, 350, and 500 μm at 3′ resolution toward the Vela C molecular complex with N(H) from $10^{21.7}$ to $10^{23.3}$ cm^{-2} also suggests a trend of HRO similar to that in the Planck results (Soler et al. 2017).

The $C_{\rm HRO}$ and $X_{\rm HRO}$ of the DR21 filament and the Serpens Main region for $N(\mathrm{H}) < 10^{23}$ cm^{-2} are -0.23 and 21.2, consistent with the values of other molecular clouds in the same density regime. The observed change in the HRO from mostly parallel alignment between magnetic fields and subfilaments of diffuse gas to mostly perpendicular alignment between magnetic fields and dense filaments of clouds is consistent with recent simulations of MHD turbulence with strong magnetic fields, indicating that magnetic fields play a significant role in structuring the interstellar medium in and around molecular clouds (Soler et al. 2013; Soler & Hennebelle 2017). Yet, there are two features in Figure 12 that are different to the HROs of most molecular clouds. First,

because the angular resolution of POL-2 is higher than other single-dish polarimeters, the HROs of the DR21 filament and the Serpens Main region trace the highest $N(\mathrm{H})$ of 10^{24} cm^{-2}. Second, the ξ of the DR21 filament and the Serpens Main region reaches a minimum between -0.6 and -0.8, which is lower than in other molecular clouds, except for the HRO of Musca obtained from Herschel and Planck data in Soler (2019). Considering that a perfectly perpendicular alignment between magnetic field and filament would give $\xi = -1$, it seems reasonable for high angular resolution observations to obtain a ξ close to -1 in a high-density filament, such as the DR21 filament.

For $N(\mathrm{H}) > 10^{23}$ cm^{-2}, Figure 12 shows a tentative positive slope in ξ versus $N(\mathrm{H})$ in both the DR21 filament and the Serpens Main region. Similar trends of positive slopes in high $N(\mathrm{H})$ regimes can be found in the HROs of Lupus I, Musca, Perseus, and Vela C South-Nest (Soler et al. 2017; Soler 2019). Statistical studies of magnetic fields in star-forming cores suggest that the small-scale magnetic fields of cores are neither simply aligned with the large-scale magnetic fields of filaments nor simply aligned with the major axes of filaments (Koch et al. 2014; Zhang et al. 2014). Therefore, the tentative positive slope in the high $N(\mathrm{H})$ regime of the HRO may indicate the transition from preferentially perpendicular alignment between filaments and magnetic fields to complex structure of the alignment between dense cores and magnetic fields. Characterizing HROs with high angular resolution submillimeter polarimeters such as POL-2 or HAWC+, which are capable of probing magnetic fields in high-density filaments, will be helpful in deciphering the role of magnetic fields in the evolution from filaments to star-forming cores.

6. Conclusions

We present JCMT POL-2 850 μm polarization observations of the DR21 filament. With the Planck 850 μm dust polarization data, we were able to characterize the magnetic field structures from the surrounding ambient gas to the DR21 filament at scales from 10 to 0.1 pc. Our main results are the following:

1. The POL-2 data reveal ordered parsec-scale magnetic fields that are perpendicular to the DR21 main filament and parallel to the subfilaments. The magnetic fields of the subfilaments appear to smoothly connect to the magnetic fields of the main filament. The magnetic fields revealed in the Planck data are well-aligned with those of the POL-2 data, indicating a smooth variation of magnetic fields from large to small scales.
2. The comparison of the total and polarized flux of the POL-2 and Planck data indicates that the missing flux issue of the POL-2 DR21 observations is more severe in Stokes I data than Stokes Q and U data. In addition, the large polarization fractions ($\gg$20%) of POL-2 low-intensity data and the preferentially large polarization fractions of POL-2 data than SCUPOL data can be explained by the Stokes I missing flux.
3. We find a power index α of 0.30–0.34 of the correlation between the polarization fractions and Stokes I intensities of POL-2 data. The α value is consistent with those inferred from the POL-2 observations toward massive star-forming regions Orion B and NGC 6334 but shallower than the POL-2 observations toward less-massive clouds, suggesting that the dust grain alignment efficiency of DR21 main filament is strongly influenced by the stellar radiation from the newborn stars.
4. The analysis of the angular dispersion functions of dust polarization yields B_{pos} of 0.6–1.0 mG in the DR21 filament and $\sim$0.1 mG in the surrounding ambient gas. The material is found to be magnetically supercritical in the filament and slightly subcritical to nearly critical in the ambient gas, consistent with the observed global infall motions of the DR21 filament. The subfilaments might be the places where the transition from subcriticality to supercriticality occurs.
5. The histogram of relative orientations between the density gradient and the magnetic field of the DR21 filament decreases with increasing $N(\mathrm{H})$ from no preferred alignment in the low-density ambient gas to mostly perpendicular in the high-density filament, in agreement with the HROs in other clouds. Owing to the high angular resolution of POL-2, we are able to trace the HRO in the highest $N(\mathrm{H})$ regime to date. A tentative positive slope of the HRO in the high-density DR21 filament is also found, as suggested from the complex magnetic field structures of the star-forming cores in the filament.

In summary, the analyses including the B_{pos}, magnetic criticality, and histogram of relative orientations are all in good agreement with recent MHD simulations of a strongly magnetized medium, suggesting that magnetic fields play an important role in shaping the main filament and subfilaments of the DR21 region.

The James Clerk Maxwell Telescope is operated by the East Asian Observatory on behalf of the National Astronomical Observatory of Japan, the Academia Sinica Institute of Astronomy and Astrophysics, the Korea Astronomy and Space Science Institute, and the Center for Astronomical Mega-Science. Additional funding support is provided by the Science and Technology Facilities Council of the United Kingdom and participating universities in the United Kingdom, Canada, and Ireland. Additional funds for the construction of SCUBA-2 and POL-2 were provided by the Canada Foundation for Innovation. The authors wish to recognize and acknowledge the very significant cultural role and reverence that the summit of Maunakea has always had within the indigenous Hawaiian community. We are most fortunate to have the opportunity to conduct observations from this mountain.

This work is supported by National Natural Science Foundation of China (NSFC) grant Nos. 11988101, U1931117, 11725313, and 12073061 and the CAS International Partnership Program of Chinese Academy of Sciences grant No. 114A11KYSB20160008. T.-C.C. is funded by Chinese Academy of Sciences Taiwan Young Talent Program grant No. 2018TW2JB0002. T.-C.C. and C.E. were supported by Special Funding for Advanced Users, budgeted and administrated by Center for Astronomical Mega-Science (CAMS), Chinese Academy of Sciences. K.P. is a Royal Society University Research Fellow, supported by grant No. URF\R1\211322. D.J. is supported by the National Research Council of Canada and by a Natural Sciences and Engineering Research Council of Canada (NSERC) Discovery Grant. P.M.K. is supported by the Ministry of Science and Technology (MoST) in Taiwan through grants 109-2112-M-001-022 and 110-2112-M-001-057.

C.W.L. is supported by the Basic Science Research Program through the National Research Foundation of Korea (NRF) funded by the Ministry of Education, Science and Technology (NRF-2019R1A2C1010851), and by the Korea Astronomy and Space Science Institute grant funded by the Korea government (MSIT; Project No. 2022-1-840-05). T.H. is supported by the National Research Foundation of Korea (NRF) grant funded by the Korea government (MSIT) through the Mid-career Research Program (2019R1A2C1087045). W.K. was supported by the NRF grant funded by the MSIT (2021R1F1A1061794). C.E. acknowledges the financial support from grant RJF/2020/000071 as a part of Ramanujan Fellowship awarded by the Science and Engineering Research Board (SERB), Department of Science and Technology (DST), Govt. of India. F.P. acknowledges support from the Spanish State Research Agency (AEI) under grant No. PID2019-105552RB-C43. M.T. is supported by JSPS KAKENHI grant Nos. 18H05442, 15H02063, and 22000005. J.K. is supported by JSPS KAKENHI grant No. 19K14775. L.F. and F.K. acknowledge the support by the MoST in Taiwan through grant 107-2119-M-001-031-MY3 and Academia Sinica through grant AS-IA-106-M03. L.F. acknowledges the support by the MoST in Taiwan through grants 111-2811-M-005-007 and 109-2112-M-005-003-MY3. C.L.H.H. acknowledges the support of the NAOJ Fellowship and JSPS KAKENHI grants 18K13586 and 20K14527. F.K. is supported by the Spanish program Unidad de Excelencia María de Maeztu CEX2020-001058-M, financed by MCIN/AEI/10.13039/501100011033. K.Q. is partially supported by National Key R&D Program of China No. 2022YFA1603100, and acknowledges the National Natural Science Foundation of China (NSFC) grant U1731237. S.P.L. acknowledges grants from the Ministry of Science and Technology of Taiwan 106-2119-M-007-021-MY3 and 109-2112-M-007-010-MY3. Y.D. acknowledges the support of JSPS KAKENHI grants 25247016 and 18H01250. Y.S.D. is supported by the National Key R&D Program of China for grant No. 2022YFA1605300, and NSFC grants Nos. 12273051, 11933003.

Appendix
The Transformation of a Position Angle from Galactic Coordinate to Equatorial Coordinate

In the IAU convention, the orientation of a position angle and a polarization angle is measured from the north and positively toward the east. At a position P on the sky, the position angle measured in galactic coordinates ($\mathrm{PA_{GA}}$) is different from the position angle measured in equatorial coordinates ($\mathrm{PA_{EQ}}$) by the angle ψ between the galactic north pole (N_{GA}) and the equatorial north pole (N_{EQ}) as

$$\mathrm{PA_{EQ}} = \mathrm{PA_{GA}} - \psi. \tag{A1}$$

According to spherical trigonometry, ψ can be derived with two sides and an opposite angle given (Figure 13). That is, with the side $\overline{N_{\mathrm{GA}}N_{\mathrm{EQ}}} = b_{N_{\mathrm{GA}}} - b_{N_{\mathrm{EQ}}}$, the side $\overline{N_{\mathrm{GA}}P} = b_{N_{\mathrm{GA}}} - b_P$, and the angle $\angle N_{\mathrm{EQ}}N_{\mathrm{GA}}P = l_{N_{\mathrm{EQ}}} - l_P$,

$$\tan(\psi) = \frac{\sin(b_{N_{\mathrm{GA}}} - b_{N_{\mathrm{EQ}}})\sin(l_{N_{\mathrm{EQ}}} - l_P)}{\sin(b_{N_{\mathrm{GA}}} - b_P)\cos(b_{N_{\mathrm{GA}}} - b_{N_{\mathrm{EQ}}}) - \cos(b_{N_{\mathrm{GA}}} - b_P)\sin(b_{N_{\mathrm{GA}}} - b_{N_{\mathrm{EQ}}})\cos(l_{N_{\mathrm{EQ}}} - l_P)}, \tag{A2}$$

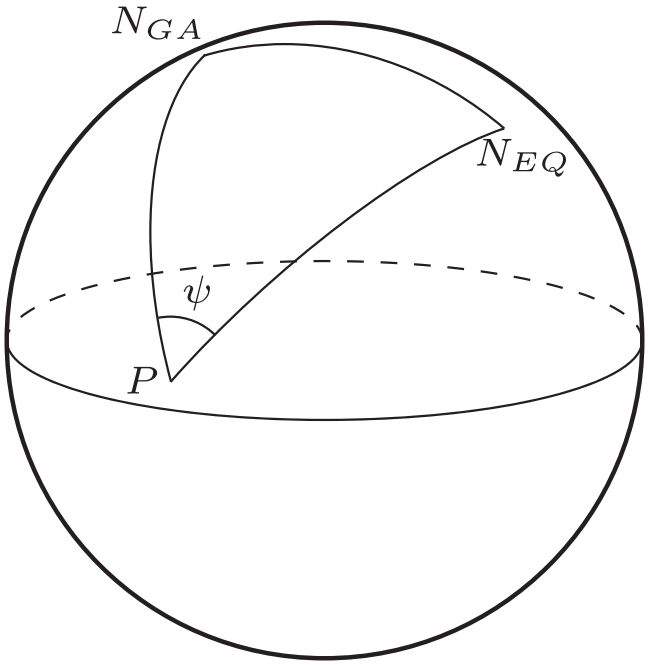

Figure 13. Illustration of the angle ψ and the spherical triangle of N_{GA}, N_{EQ}, and P.

where $b_{N_{\mathrm{GA}}}$, $b_{N_{\mathrm{EQ}}}$, $l_{N_{\mathrm{EQ}}}$, b_P, and l_P are the galactic latitudes and longitudes of N_{GA}, N_{EQ}, and P. After substituting $b_{N_{\mathrm{GA}}} = 90°$, $b_{N_{\mathrm{EQ}}} = 27.^{\circ}1$, $l_{N_{\mathrm{EQ}}} = 122.^{\circ}9$ for epoch J2000 and some algebraic manipulations,

$$\psi = \arctan\left[\frac{\cos(l_P - 32.^{\circ}9)}{\cos b_P \cot 62.^{\circ}9 - \sin b_P \sin(l_P - 32.^{\circ}9)}\right]. \tag{A3}$$

ORCID iDs

Tao-Chung Ching https://orcid.org/0000-0001-8516-2532
Keping Qiu https://orcid.org/0000-0002-5093-5088
Di Li https://orcid.org/0000-0003-3010-7661
Zhiyuan Ren https://orcid.org/0000-0003-4659-1742
Shih-Ping Lai https://orcid.org/0000-0001-5522-486X
David Berry https://orcid.org/0000-0001-6524-2447
Kate Pattle https://orcid.org/0000-0002-8557-3582
Ray Furuya https://orcid.org/0000-0003-0646-8782
Derek Ward-Thompson https://orcid.org/0000-0003-1140-2761
Doug Johnstone https://orcid.org/0000-0002-6773-459X
Patrick M. Koch https://orcid.org/0000-0003-2777-5861
Chang Won Lee https://orcid.org/0000-0002-3179-6334
Thiem Hoang https://orcid.org/0000-0003-2017-0982
Tetsuo Hasegawa https://orcid.org/0000-0003-1853-0184
Woojin Kwon https://orcid.org/0000-0003-4022-4132
Pierre Bastien https://orcid.org/0000-0002-0794-3859
Chakali Eswaraiah https://orcid.org/0000-0003-4761-6139

Jia-Wei Wang https://orcid.org/0000-0002-6668-974X
Kyoung Hee Kim https://orcid.org/0000-0001-9597-7196
Jihye Hwang https://orcid.org/0000-0001-7866-2686
Archana Soam https://orcid.org/0000-0002-6386-2906
A-Ran Lyo https://orcid.org/0000-0002-9907-8427
Junhao Liu https://orcid.org/0000-0002-4774-2998
Valentin J. M. Le Gouellec https://orcid.org/0000-0002-5714-799X
Doris Arzoumanian https://orcid.org/0000-0002-1959-7201
Anthony Whitworth https://orcid.org/0000-0002-1178-5486
James Di Francesco https://orcid.org/0000-0002-9289-2450
Frédérick Poidevin https://orcid.org/0000-0002-5391-5568
Tie Liu https://orcid.org/0000-0002-5286-2564
Simon Coudé https://orcid.org/0000-0002-0859-0805
Mehrnoosh Tahani https://orcid.org/0000-0001-8749-1436
Hong-Li Liu https://orcid.org/0000-0003-3343-9645
Takashi Onaka https://orcid.org/0000-0002-8234-6747
Motohide Tamura https://orcid.org/0000-0002-6510-0681
Zhiwei Chen https://orcid.org/0000-0003-0849-0692
Xindi Tang https://orcid.org/0000-0002-4154-4309
Florian Kirchschlager https://orcid.org/0000-0002-3036-0184
Tyler L. Bourke https://orcid.org/0000-0001-7491-0048
Do-Young Byun https://orcid.org/0000-0003-1157-4109
Huei-Ru Vivien Chen https://orcid.org/0000-0002-9774-1846
Wen Ping Chen https://orcid.org/0000-0003-0262-272X
Jungyeon Cho https://orcid.org/0000-0003-1725-4376
Antonio Chrysostomou https://orcid.org/0000-0002-9583-8644
Eun Jung Chung https://orcid.org/0000-0003-0014-1527
Y. Sophia Dai https://orcid.org/0000-0002-7928-416X
Pham Ngoc Diep https://orcid.org/0000-0002-2808-0888
Yasuo Doi https://orcid.org/0000-0001-8746-6548
Hao-Yuan Duan https://orcid.org/0000-0002-7022-4742
David Eden https://orcid.org/0000-0002-5881-3229
Lapo Fanciullo https://orcid.org/0000-0001-9930-9240
Laura M. Fissel https://orcid.org/0000-0002-4666-609X
Erica Franzmann https://orcid.org/0000-0003-2142-0357
Per Friberg https://orcid.org/0000-0002-8010-8454
Rachel Friesen https://orcid.org/0000-0001-7594-8128
Gary Fuller https://orcid.org/0000-0001-8509-1818
Tim Gledhill https://orcid.org/0000-0002-2859-4600
Sarah Graves https://orcid.org/0000-0001-9361-5781
Jane Greaves https://orcid.org/0000-0002-3133-413X
Qilao Gu https://orcid.org/0000-0002-2826-1902
Saeko Hayashi https://orcid.org/0000-0001-5026-490X
Martin Houde https://orcid.org/0000-0003-4420-8674
Charles L. H. Hull https://orcid.org/0000-0002-8975-7573
Tsuyoshi Inoue https://orcid.org/0000-0002-7935-8771
Shu-ichiro Inutsuka https://orcid.org/0000-0003-4366-6518
Il-Gyo Jeong https://orcid.org/0000-0002-5492-6832
Vera Könyves https://orcid.org/0000-0002-3746-1498
Ji-hyun Kang https://orcid.org/0000-0001-7379-6263
Miju Kang https://orcid.org/0000-0002-5016-050X
Janik Karoly https://orcid.org/0000-0001-5996-3600
Akimasa Kataoka https://orcid.org/0000-0003-4562-4119
Koji Kawabata https://orcid.org/0000-0001-6099-9539
Francisca Kemper https://orcid.org/0000-0003-2743-8240
Jongsoo Kim https://orcid.org/0000-0002-1229-0426
Shinyoung Kim https://orcid.org/0000-0001-9333-5608
Kee-Tae Kim https://orcid.org/0000-0003-2412-7092
Gwanjeong Kim https://orcid.org/0000-0003-2011-8172
Jason Kirk https://orcid.org/0000-0002-4552-7477
Masato I. N. Kobayashi https://orcid.org/0000-0003-3990-1204
Takayoshi Kusune https://orcid.org/0000-0002-9218-9319
Jungmi Kwon https://orcid.org/0000-0003-2815-7774
Kevin Lacaille https://orcid.org/0000-0001-9870-5663
Chi-Yan Law https://orcid.org/0000-0003-1964-970X
Sang-Sung Lee https://orcid.org/0000-0002-6269-594X
Hyeseung Lee https://orcid.org/0000-0003-3465-3213
Jeong-Eun Lee https://orcid.org/0000-0003-3119-2087
Chin-Fei Lee https://orcid.org/0000-0002-3024-5864
Yong-Hee Lee https://orcid.org/0000-0001-6047-701X
Guangxing Li https://orcid.org/0000-0003-3144-1952
Hua-bai Li https://orcid.org/0000-0003-2641-9240
Sheng-Jun Lin https://orcid.org/0000-0002-6868-4483
Sheng-Yuan Liu https://orcid.org/0000-0003-4603-7119
Xing Lu https://orcid.org/0000-0003-2619-9305
Steve Mairs https://orcid.org/0000-0002-6956-0730
Masafumi Matsumura https://orcid.org/0000-0002-6906-0103
Brenda Matthews https://orcid.org/0000-0003-3017-9577
Gerald Moriarty-Schieven https://orcid.org/0000-0002-0393-7822
Tetsuya Nagata https://orcid.org/0000-0001-9264-9015
Fumitaka Nakamura https://orcid.org/0000-0001-5431-2294
Nguyen Bich Ngoc https://orcid.org/0000-0002-5913-5554
Nagayoshi Ohashi https://orcid.org/0000-0003-0998-5064
Geumsook Park https://orcid.org/0000-0001-8467-3736
Harriet Parsons https://orcid.org/0000-0002-6327-3423
Tae-Soo Pyo https://orcid.org/0000-0002-3273-0804
Lei Qian https://orcid.org/0000-0003-0597-0957
Ramprasad Rao https://orcid.org/0000-0002-1407-7944
Mark Rawlings https://orcid.org/0000-0002-6529-202X
Jonathan Rawlings https://orcid.org/0000-0001-5560-1303
John Richer https://orcid.org/0000-0002-9693-6860
Andrew Rigby https://orcid.org/0000-0002-3351-2200
Giorgio Savini https://orcid.org/0000-0003-4449-9416
Yoshito Shimajiri https://orcid.org/0000-0001-9368-3143
Hiroko Shinnaga https://orcid.org/0000-0001-9407-6775
Ya-Wen Tang https://orcid.org/0000-0002-0675-276X
Kohji Tomisaka https://orcid.org/0000-0003-2726-0892
Le Ngoc Tram https://orcid.org/0000-0002-6488-8227
Serena Viti https://orcid.org/0000-0001-8504-8844
Hongchi Wang https://orcid.org/0000-0003-0746-7968
Jintai Wu https://orcid.org/0000-0001-7276-3590
Jinjin Xie https://orcid.org/0000-0002-2738-146X
Hsi-Wei Yen https://orcid.org/0000-0003-1412-893X
Hyunju Yoo https://orcid.org/0000-0002-8578-1728
Hyeong-Sik Yun https://orcid.org/0000-0001-6842-1555
Chuan-Peng Zhang https://orcid.org/0000-0002-4428-3183
Yapeng Zhang https://orcid.org/0000-0002-5102-2096
Jianjun Zhou https://orcid.org/0000-0003-0356-818X
Philippe André https://orcid.org/0000-0002-3413-2293
Sam Falle https://orcid.org/0000-0002-9829-0426
Jean-François Robitaille https://orcid.org/0000-0001-5079-8573
Sven van Loo https://orcid.org/0000-0003-4746-8500

References

Alves, F. O., Franco, G. A. P., & Girart, J. M. 2008, A&A, 486, L13
Andersson, B.-G., Lazarian, A., & Vaillancourt, J. E. 2015, ARA&A, 53, 501
André, P., Di Francesco, J., Ward-Thompson, D., et al. 2014, in Protostars and Planets VI, ed. H. Beuther et al. (Tucson, AZ: Univ. Arizona Press), 27
Argon, A. L., Reid, M. J., & Menten, K. M. 2000, ApJS, 129, 159
Arzoumanian, D., André, P., Didelon, P., et al. 2011, A&A, 529, L6
Arzoumanian, D., Furuya, R. S., Hasegawa, T., et al. 2021, A&A, 647, A78
Bastien, P., Bissonnette, E., Simon, A., et al. 2011, in ASP Conf. Ser. 449, Astronomical Polarimetry 2008: Science from Small to Large Telescopes, 449 (San Francisco, CA: ASP), 68
Braz, M. A., & Epchtein, N. 1983, A&AS, 54, 167
Cao, Y., Qiu, K., Zhang, Q., et al. 2019, ApJS, 241, 1
Chandrasekhar, S., & Fermi, E. 1953, ApJ, 118, 113
Chapman, N. L., Goldsmith, P. F., Pineda, J. L., et al. 2011, ApJ, 741, 21
Chen, C.-Y., Li, Z.-Y., King, P. K., & Fissel, L. M. 2017, ApJ, 847, 140
Chen, C.-Y., & Ostriker, E. C. 2014, ApJ, 785, 69
Ching, T.-C., Lai, S.-P., Zhang, Q., et al. 2017, ApJ, 838, 121
Ching, T.-C., Lai, S.-P., Zhang, Q., et al. 2018, ApJ, 865, 110
Chuss, D. T., Andersson, B.-G., Bally, J., et al. 2019, ApJ, 872, 187
Corradi, R. L. M., Aznar, R., & Mampaso, A. 1998, MNRAS, 297, 617s
Coudé, S., Bastien, P., Houde, M., et al. 2019, ApJ, 877, 88
Cox, N. L. J., Arzoumanian, D., André, P., et al. 2016, A&A, 590, A110
Crutcher, R. M. 2012, ARA&A, 50, 29
Crutcher, R. M., Nutter, D. J., Ward-Thompson, D., et al. 2004, ApJ, 600, 279
Crutcher, R. M., Troland, T. H., Lazareff, B., Paubert, G., & Kazès, I. 1999, ApJL, 514, L121
Csengeri, T., Bontemps, S., Schneider, N., Motte, F., & Dib, S. 2011, A&A, 527, A135
Currie, M. J., Berry, D. S., Jenness, T., et al. 2014, in ASP Conf. Ser. 485, Astronomical Data Analysis Software and Systems XXIII (San Francisco, CA: ASP), 391
Davis, C. J., Kumar, M. S. N., Sandell, G., et al. 2007, MNRAS, 374, 29
Davis, C. J., & Smith, M. D. 1996, A&A, 310, 961
Davis, L. 1951, PhRv, 81, 890
Dempsey, J. T., Friberg, P., Jenness, T., et al. 2013, MNRAS, 430, 2534
Doi, Y., Hasegawa, T., Furuya, R. S., et al. 2020, ApJ, 899, 28
Doi, Y., Tomisaka, K., Hasegawa, T., et al. 2021, ApJL, 923, L9
Dotson, J. L., Davidson, J., Dowell, C. D., et al. 2000, ApJS, 128, 335
Dotson, J. L., Vaillancourt, J. E., Kirby, L., et al. 2010, ApJS, 186, 406
Downes, D., & Rinehart, R. 1966, ApJ, 144, 937
Draine, B. T., & Fraisse, A. A. 2009, ApJ, 696, 1
Duarte-Cabral, A., Bontemps, S., Motte, F., et al. 2013, A&A, 558, A125
Duarte-Cabral, A., Bontemps, S., Motte, F., et al. 2014, A&A, 570, A1
Eswaraiah, C., Li, D., Furuya, R. S., et al. 2021, ApJL, 912, L27
Eswaraiah, C., Li, D., Samal, M. R., et al. 2020, ApJ, 897, 90
Falgarone, E., Troland, T. H., Crutcher, R. M., & Paubert, G. 2008, A&A, 487, 247
Fanciullo, L., Kemper, F., Pattle, K., et al. 2022, MNRAS, 512, 1985
Fernández-López, M., Arce, H. G., Looney, L., et al. 2014, ApJL, 790, L19
Fissel, L. M., Ade, P. A. R., Angilè, F. E., et al. 2019, ApJ, 878, 110
Friberg, P., Bastien, P., Berry, D., et al. 2016, Proc. SPIE, 9914, 991403
Galván-Madrid, R., Zhang, Q., Keto, E., et al. 2010, ApJ, 725, 17
Girart, J. M., Frau, P., Zhang, Q., et al. 2013, ApJ, 772, 69
Glenn, J., Walker, C. K., & Young, E. T. 1999, ApJ, 511, 812
Goodman, A. A., Bastien, P., Myers, P. C., & Menard, F. 1990, ApJ, 359, 363
Greaves, J. S., Holland, W. S., Minchin, N. R., Murray, A. G., & Stevens, J. A. 1999, A&A, 344, 668
Guerra, J. A., Chuss, D. T., Dowell, C. D., et al. 2021, ApJ, 908, 98
Hacar, A., Tafalla, M., Forbrich, J., et al. 2018, A&A, 610, A77
Hacar, A., Tafalla, M., Kauffmann, J., & Kovács, A. 2013, A&A, 554, A55
Heitsch, F., Zweibel, E. G., Mac Low, M.-M., Li, P., & Norman, M. L. 2001, ApJ, 561, 800
Hennemann, M., Motte, F., Schneider, N., et al. 2012, A&A, 543, L3
Heyer, M., Gong, H., Ostriker, E., & Brunt, C. 2008, ApJ, 680, 420
Hildebrand, R. H., Kirby, L., Dotson, J. L., Houde, M., & Vaillancourt, J. E. 2009, ApJ, 696, 567
Hill, T., Motte, F., Didelon, P., et al. 2011, A&A, 533, A94
Hoang, T., & Lazarian, A. 2016, ApJ, 831, 159
Hoang, T., Tram, L. N., Lee, H., Diep, P. N., & Ngoc, N. B. 2021, ApJ, 908, 218
Holland, W. S., Bintley, D., Chapin, E. L., et al. 2013, MNRAS, 430, 2513
Houde, M., Vaillancourt, J. E., Hildebrand, R. H., Chitsazzadeh, S., & Kirby, L. 2009, ApJ, 706, 1504
Hu, B., Qiu, K., Cao, Y., et al. 2021, ApJ, 908, 70
Hwang, J., Kim, J., Pattle, K., et al. 2021, ApJ, 913, 85
Hwang, J., Kim, J., Pattle, K., et al. 2022, ApJ, 941, 51
Inoue, T., & Fukui, Y. 2013, ApJL, 774, L31
Itoh, Y., Chrysostomou, A., Burton, M., et al. 1999, MNRAS, 304, 406
Jenness, T., Chapin, E. L., Berry, D. S., et al. 2013, SMURF: SubMillimeter User Reduction Facility, Astrophysics Source Code Library, ascl:1310.007
Kirby, L. 2009, ApJ, 694, 1056
Kirk, J. M., Ward-Thompson, D., Palmeirim, P., et al. 2013, MNRAS, 432, 1424
Koch, E. W., & Rosolowsky, E. W. 2015, MNRAS, 452, 3435
Koch, P. M., Tang, Y.-W., & Ho, P. T. P. 2012, ApJ, 747, 79
Koch, P. M., Tang, Y.-W., & Ho, P. T. P. 2013, ApJ, 775, 77
Koch, P. M., Tang, Y.-W., Ho, P. T. P., et al. 2014, ApJ, 797, 99
Koch, P. M., Tang, Y.-W., Ho, P. T. P., et al. 2018, ApJ, 855, 39
Könyves, V., André, P., Men'shchikov, A., et al. 2015, A&A, 584, A91
Könyves, V., Ward-Thompson, D., Pattle, K., et al. 2021, ApJ, 913, 57
Kumar, M. S. N., Davis, C. J., Grave, J. M. C., Ferreira, B., & Froebrich, D. 2007, MNRAS, 374, 54
Kumar, M. S. N., Palmeirim, P., Arzoumanian, D., & Inutsuka, S. I. 2020, A&A, 642, A87
Kwon, J., Doi, Y., Tamura, M., et al. 2018, ApJ, 859, 4
Kwon, W., Pattle, K., Sadavoy, S., et al. 2022, ApJ, 926, 163
Lai, S.-P., Girart, J. M., & Crutcher, R. M. 2003, ApJ, 598, 392
Lazarian, A., & Hoang, T. 2007, MNRAS, 378, 910
Li, H.-b., Yuen, K. H., Otto, F., et al. 2015, Natur, 520, 518
Li, P. S., & Klein, R. I. 2019, MNRAS, 485, 4509
Liu, H. B., Jiménez-Serra, I., Ho, P. T. P., et al. 2012, ApJ, 756, 10
Liu, J., Qiu, K., Berry, D., et al. 2019, ApJ, 877, 43
Liu, J., Zhang, Q., Commercon, B., et al. 2021, ApJ, 919, 79
Liu, T., Li, P. S., Juvela, M., et al. 2018, ApJ, 859, 151
Lyo, A.-R., Kim, J., Sadavoy, S., et al. 2021, ApJ, 918, 85
Mairs, S., Dempsey, J. T., Bell, G. S., et al. 2021, AJ, 162, 191
Malinen, J., Montier, L., Montillaud, J., et al. 2016, MNRAS, 460, 1934
Matthews, B. C., McPhee, C. A., Fissel, L. M., & Curran, R. L. 2009, ApJS, 182, 143
Matthews, T. G., Ade, P. A. R., Angilè, F. E., et al. 2014, ApJ, 784, 116
Minchin, N. R., & Murray, A. G. 1994, A&A, 286, 579
Molinari, S., Swinyard, B., Bally, J., et al. 2010, A&A, 518, L100
Motte, F., Bontemps, S., Schilke, P., et al. 2007, A&A, 476, 1243
Mouschovias, T. C., & Ciolek, G. E. 1999, in The Origin of Stars and Planetary Systems, NATO ASI Ser. C, ed. C. J. Lada & N. D. Kylafis, Vol. 540 (Berlin: Springer), 305
Naghizadeh-Khouei, J., & Clarke, D. 1993, A&A, 274, 968
Nakamura, F., & Li, Z.-Y. 2008, ApJ, 687, 354
Ngoc, N. B., Diep, P. N., Parsons, H., et al. 2021, ApJ, 908, 10
Ossenkopf, V., & Henning, T. 1994, A&A, 291, 943
Ostriker, E. C., Stone, J. M., & Gammie, C. F. 2001, ApJ, 546, 980
Padoan, P., Goodman, A., Draine, B. T., et al. 2001, ApJ, 559, 1005
Palau, A., Zhang, Q., Girart, J. M., et al. 2021, ApJ, 912, 159
Palmeirim, P., André, P., Kirk, J., et al. 2013, A&A, 550, A38
Parsons, H. A. L., Berry, D. S., Rawlings, M. G., & Graves, S. F. 2018, The POL-2 Data Reduction Cookbook 1.0, Starlink Project (Hilo, HI: East Asian Observatory), http://starlink.eao.hawaii.edu/docs/sc22.pdf
Pattle, K., Lai, S.-P., Hasegawa, T., et al. 2019, ApJ, 880, 27
Pattle, K., Ward-Thompson, D., Berry, D., et al. 2017, ApJ, 846, 122
Pattle, K., Ward-Thompson, D., Hasegawa, T., et al. 2018, ApJL, 860, L6
Pattle, K., Ward-Thompson, D., Kirk, J. M., et al. 2015, MNRAS, 450, 1094
Peretto, N., Fuller, G. A., Duarte-Cabral, A., et al. 2013, A&A, 555, A112
Pestalozzi, M. R., Minier, V., & Booth, R. S. 2005, A&A, 432, 737
Planck Collaboration, Adam, R., Ade, P. A. R., et al. 2016a, A&A, 586, A135
Planck Collaboration, Ade, P. A. R., Aghanim, N., et al. 2015, A&A, 576, A104
Planck Collaboration, Ade, P. A. R., Aghanim, N., et al. 2016b, A&A, 586, A138
Planck Collaboration, Aghanim, N., Akrami, Y., et al. 2020, A&A, 641, A12
Planck Collaboration I, Adam, R., Ade, P. A. R., et al. 2016, A&A, 594, A1
Planck Collaboration VIII, Adam, R., Ade, P. A. R., et al. 2016, A&A, 594, A8
Planck Collaboration XI, Abergel, A., Ade, P. A. R., et al. 2014, A&A, 571, A11
Poidevin, F., Bastien, P., & Matthews, B. C. 2010, ApJ, 716, 893
Poidevin, F., Falceta-Gonçalves, D., Kowal, G., de Gouveia Dal Pino, E., & Mário Magalhães, A. 2013, ApJ, 777, 112
Roberts, D. A., Dickel, H. R., & Goss, W. M. 1997, ApJ, 476, 209
Rygl, K. L. J., Brunthaler, A., Sanna, A., et al. 2012, A&A, 539, A79
Schleuning, D. A. 1998, ApJ, 493, 811

Schneider, N., Bontemps, S., Motte, F., et al. 2016, A&A, 591, A40
Schneider, N., Csengeri, T., Bontemps, S., et al. 2010, A&A, 520, A49
Schneider, N., Csengeri, T., Hennemann, M., et al. 2012, A&A, 540, L11
Shu, F. H., Adams, F. C., & Lizano, S. 1987, ARA&A, 25, 23
Soam, A., Liu, T., Andersson, B.-G., et al. 2019, ApJ, 883, 95
Soam, A., Pattle, K., Ward-Thompson, D., et al. 2018, ApJ, 861, 65
Soler, J. D. 2019, A&A, 629, A96
Soler, J. D., Ade, P. A. R., Angilè, F. E., et al. 2017, A&A, 603, A64
Soler, J. D., Alves, F., Boulanger, F., et al. 2016, A&A, 596, A93
Soler, J. D., & Hennebelle, P. 2017, A&A, 607, A2
Soler, J. D., Hennebelle, P., Martin, P. G., et al. 2013, ApJ, 774, 128
Sugitani, K., Nakamura, F., Watanabe, M., et al. 2011, ApJ, 734, 63
Tamura, M., Nagata, T., Sato, S., & Tanaka, M. 1987, MNRAS, 224, 413
Tritsis, A., & Tassis, K. 2018, Sci, 360, 635
Vallée, J. P., & Fiege, J. D. 2006, ApJ, 636, 332
Wang, J.-W., Lai, S.-P., Clemens, D. P., et al. 2020, ApJ, 888, 13
Wang, J.-W., Lai, S.-P., Eswaraiah, C., et al. 2019, ApJ, 876, 42
Ward-Thompson, D., Pattle, K., Bastien, P., et al. 2017, ApJ, 842, 66
White, G. J., Abergel, A., Spencer, L., et al. 2010, A&A, 518, L114
Yen, H.-W., Koch, P. M., Hull, C. L. H., et al. 2021, ApJ, 907, 33
Zapata, L. A., Loinard, L., Su, Y.-N., et al. 2012, ApJ, 744, 86
Zapata, L. A., Schmid-Burgk, J., Pérez-Goytia, N., et al. 2013, ApJL, 765, L29
Zhang, Q., Qiu, K., Girart, J. M., et al. 2014, ApJ, 792, 116